Natural suspended particulate matter (SPM) versus lab-controlled particles: Comparison of the reactivity and association mode of Zn

Mathieu Le Meur, Emmanuelle Montargès-Pelletier, Renaud Gley, Valérie Briois, Laurent Michot, Hussein Kanbar, Céline Caillet, Angelina Razafitianamaharavo, Frédéric Villiéras

▶ **To cite this version:**

Mathieu Le Meur, Emmanuelle Montargès-Pelletier, Renaud Gley, Valérie Briois, Laurent Michot, et al.. Natural suspended particulate matter (SPM) versus lab-controlled particles: Comparison of the reactivity and association mode of Zn. Applied Geochemistry, 2022, pp.105286. 10.1016/j.apgeochem.2022.105286 . hal-03627844

HAL Id: hal-03627844
https://hal.univ-lorraine.fr/hal-03627844

Submitted on 20 Nov 2022

HAL is a multi-disciplinary open access archive for the deposit and dissemination of scientific research documents, whether they are published or not. The documents may come from teaching and research institutions in France or abroad, or from public or private research centers.

L'archive ouverte pluridisciplinaire **HAL**, est destinée au dépôt et à la diffusion de documents scientifiques de niveau recherche, publiés ou non, émanant des établissements d'enseignement et de recherche français ou étrangers, des laboratoires publics ou privés.

Distributed under a Creative Commons Attribution - NonCommercial - NoDerivatives 4.0 International License

Natural Suspended Particulate Matter (SPM) versus lab controlled particles: comparison of reactivity and association mode of Zn.

Mathieu LE MEUR[1,2], Emmanuelle MONTARGES-PELLETIER[1, 2,*], Renaud GLEY[1], Valérie BRIOIS[3], Laurent MICHOT[4], Hussein KANBAR[1,2] Céline CAILLET[1], Angelina RAZAFITIANAMAHARAVO[1], Frédéric VILLIERAS[1]

[1] *Université de Lorraine, CNRS, LIEC, F- 54000 Nancy, France.*

[2] *LTSER Zone Atelier Moselle, F-54000 Nancy, France*

[3] *Synchrotron SOLEIL, L'Orme des Merisiers, Saint Aubin BP48, 91192 Gif sur Yvette cedex, France*

[4] *Sorbonne Université CNRS, Phenix Physicochimie des Electrolytes et Nanosystèmes InterfaciauX. 4, Place Jussieu 75005 Paris.*

** corresponding author emmanuelle.montarges@univ-lorraine.fr*

ABSTRACT

River Suspended Particulate Matter (SPM) is playing a crucial role in the fate and behavior of pollutants such as Zn, a widespread trace metal commonly encountered in continental surface waters. SPM is constituted of particles and colloids and is described as complex, heterogeneous particles composed by mineral, organic and microbiological components with high surface reactivity. In this study, the surface properties of river SPM and its capacity to bind Zn were probed using electrophoretic mobility (EM) experiments, specific surface area (SSA) measurements, Zn adsorption tests and X-ray Absorption Spectroscopy experiments (XAS). The external characteristics and reactivity of lab-controlled mineral phases (illite, Ferrihydrite, illite-iron (hydr)oxide composite, calcite) were investigated as for natural SPM. Electrophoretic mobility (EM) of the SPM exhibited low variations among the samples and was essentially assigned to the clay particles that predominate the mineralogical composition. Zn sorption experiments evidenced comparable adsorption capacity except for two samples in relation with their different mineral and chemical composition. Zn K-edge XAS data revealed that at low Zn loadings, the binding mode of this metal with environmental particles was controlled by the mineralogical composition. Indeed, Linear Combination Fitting of XAS curves, completed by shell-to-shell fitting revealed Zn association to SPM by surface complexation. XAS results showed that for SPM samples collected in high flow regime, Zn was mainly bound to clay minerals. In contrast, for the SPM sample collected during low flow regime, Zn was not only bound to clay mineral but also to iron (hydr)oxides.

Key words: Suspended Particulate Matter, River, Zn, lab-controlled minerals, surface reactivity, binding mode, X-ray absorption spectroscopy.

1. INTRODUCTION

The development of human activities since the end of the XIXth century resulted in a strong increase in the extraction of metallic ores, which provoked a strong increase of trace metal deposition in environmental media (Nriagu and Pacyna, 1988; Viers et al., 2009). Among those trace metals, Cu, Zn and Pb are the most commonly encountered worldwide and are frequently occurring in urban areas, and thus in domestic waste waters or run-off waters from artificial surfaces (roads, roofs, parking lots, pavements etc). Zinc is a common contaminant in continental rivers (Grosbois et al., 2012; Juillot et al., 2011; Le Pape et al., 2014, 2012; Priadi et al., 2012; Superville et al., 2011; Yin et al., 2015) and was found to be predominantly associated to the suspended matter (Le Meur et al., 2016; Resongles et al., 2015; Viers et al., 2009). In order to better predict Zn fate and behaviour in rivers, it is necessary to unravel the interaction between Zn and environmental particles, such as suspended particulate matter or SPM. River SPM encompass particles and colloids, and are commonly described as complex and heterogeneous aggregates composed by mineral, organic and microbiological components (Stumm, 1993). The affinity of natural surfaces towards trace metals was evidenced through metal adsorption experiments on environmental matrices, such as soils, sediments or river SPM (Bengtsson and Picado, 2008; Bibby and Webster-Brown, 2006; Buyang et al., 2019; Covelo et al., 2007; Wang et al., 1997; Young and Harvey, 1992). These studies unraveled the crucial role of particle size, morphology, composition and structural irregularities of the submicrometric constituents and repeatedly demonstrated the major role of Fe-(hydr)oxide and clay mineral surfaces. In order to better understand the affinity of natural particles towards metals such as Zn, and for establishing quantitative models to predict Zn behaviour in natural media, numerous lab-controlled investigations on model or synthetic adsorbents, under controlled conditions (pH, temperature, ionic strength, time), were thus performed to identify adsorption mechanisms and the nature of the binding mode(s) (Churakov and Dähn, 2012;

Cismasu et al., 2013; Dähn et al., 2011; Davis et al., 1998; Dyer et al., 2004; Lee et al., 2004; Miyazaki et al., 2003; Montoya et al., 2018; Nachtegaal and Sparks, 2004; Schlegel et al., 2001; Schlegel and Manceau, 2006; Sipos et al., 2018; Tertre et al., 2009; Toner et al., 2006; Trivedi et al., 2004, 2001a, 2001b). However, only a limited number of studies dealing with metal adsorption mechanisms on model mineral phases, tried to explicitly consider the complexity and heterogeneity of environmental particles.

Furthermore, a crucial question remains about the extrapolation of theoretical adsorption models obtained on pure and single mineral phases to environmental particles. Can we compare river SPM reactivity (towards Zn for instance) with that of pure mineral phases (e.g. illite, ferrihydrite, goethite, calcite)? Also, as soon as we assume that river SPM is formed of mineral assemblies, what will be the real availability of adsorption sites and reactive surface groups? Such an issue is important to address since those chemical groups might be partially involved in the mineral-mineral interactions or mineral-organic interactions (Chen et al., 2004; Zimmermann-Timm, 2002). This paper investigated River SPM reactivity towards Zn, and compared it to that of pure mineral phases including clay minerals (illite), iron (hydr)oxides (ferrihydrite and goethite) and calcite. Those mineral phases were selected since clay minerals were shown to be predominant in most continental river SPM (Manickam et al., 1985; Slomberg et al., 2016) and particularly for Moselle River SPM (Le Meur et al., 2016). In addition, to try to better approach natural complexity, the reactivity of a composite mineral obtained from the hydrolysis of iron in the presence of illite platelets was also investigated.

To provide evidence for the role of SPM components in Zn fate, Zn adsorption isotherms were interpreted regarding external characteristics such as textural properties (gas adsorption experiments), surface charge (electrophoretic mobility), or cationic exchange capacity whereas the binding modes of Zn were investigated through X-ray absorption spectroscopy experiments.

2. MATERIALS AND METHODS

2.1 Study site and SPM samples

River SPM samples were collected from Moselle River and tributaries, within the French Moselle catchment, in the north-eastern part of France. Sampling stations along the Moselle River and tributaries were selected to screen the Zn association mode in SPM, and will be referred to as follow in the text: FRO for Frouard, PSV for Pont-Saint-Vincent, MIL for Millery; PAM for Pont-a-Mousson, ARG for Argancy; FLO for Florange and THI for Thionville FRO, MIL, PAM, ARG and THI are Moselle River stations, following a gradient of urbanization of the watershed. PSV is a station on the Madon River, FLO is a station on the Fensch River Those three stations on tributaries are located close to the junction with Moselle river. More information is available in previous publications (Le Meur et al., 2017, 2016) as well as on the data repository ORDAR (appendix A https://doi.org/10.24396/ORDAR-62). Numerous SPM samples from the station Frouard or FRO on Moselle River, were collected between November 2012 and March 2015 (Table 1). For SPM collection, River water was pumped and sent to a continuous flow field centrifuge (CEPA Z-41 20000 rpm, equivalent to 17000 g). The flow rate of the pumping was set to 600 L h^{-1}. Such a collection method guaranteed the representativeness of SPM samples as up to one hundred grams were collected corresponding to 1 or 2 m^3 of centrifuged water. Turbidity and grain size distribution of river water entering and exiting the centrifuge bowl were checked during the whole sampling to assess the performance of the field centrifuge. The size cut-off of retained particles was approximately 3 µm and was checked with laser diffraction analysis of centrifuge input and output at different times during field centrifugation (laser diffraction instrument SYMPATEC). SPM were gently recovered from the Teflon plates covering the internal surface of the centrifuge bowl and were immediately frozen and freeze-dried for analytical purpose. The samples were dialyzed with ultrapure water during 2 or 3 days, until the electrical conductivity was below 5 µS cm^{-1}. The elemental

composition of SPM samples can be found in Appendix A (https://doi.org/10.24396/ORDAR-62).

2. 2. Model compounds

2.2.1. Illite purification.

The raw clay mineral sample Illite du Puy (Argile du Velay) was characterized by X-ray diffraction (XRD). XRD patterns revealed the presence of quartz, feldspar, kaolinite and calcite as the accessory minerals. Then, prior to use, the raw clay mineral sample was purified and homo-ionized with sodium (Blachier et al., 2014). A 40 g L^{-1} illite suspension was first mixed with 1M sodium acetate solution set to pH 5 by addition of acetic acid (0.1 M) to remove carbonates. After centrifugation (7,500 rpm, 45 min), the solid was exchanged three times using 1 M NaCl solution. The suspension was then dialyzed several times in deionized water until the water was chloride free (conductivity below 5 µS cm^{-1}). Clay suspension was then centrifuged in order to separate the different clay size fractions. Centrifuging during one hour with 25,700 g resulted in two size fractions referred to as illite-s2 (bottom particles) and illite-s3 (supernatant). A second centrifugation during 45 min with 34,800 g provided a smallest size fraction referred to as illite-s3bis. TEM observations on the illite-s3 and illite-s3bis fractions evidenced a rather homogeneous clay phase, in size and composition (Appendix B, supplementary information can be found there https://doi.org/10.24396/ORDAR-28). The size fraction illite-s3 was selected for the adsorption experiments and for the preparation of clay-composites with ferrihydrite.

2.2.2. Ferrihydrite synthesis.

Ferrihydrite (FeH) was synthetized following the method proposed for the 2-line FeH (Cornell and Schwertmann, 2003). Ferric solution was prepared using 0.1 M of the nitrate salt

130 $Fe(NO_3)_3.9H_2O$. A solution of KOH 1 M was added to the ferric solution to bring the pH to 8.
131 Then, the suspension was stirred for 1 h and centrifuged (10 min, 7,000 rpm). Ferrihydrite was
132 frozen and freeze-dried prior to analyses and adsorption experiments.
133
134 *2.2.3. Illite-iron (hydr)oxide composite.*
135 A clay composite, on the basis of illite and iron (hydr)oxide, was prepared to mimic the presence
136 of iron (hydr)oxide coatings evidenced on natural particles (Le Meur et al., 2016; Nachtegaal
137 and Sparks, 2004). This mixed sample was referred to as Illite-FeH, and was prepared as
138 follows: 100 mg of purified illite was suspended in 100 mL of ultra-pure water. Fe(III) nitrate
139 solution (0.001 M, pH 4) and KOH solution (0.01 M) were simultaneously added to the illite
140 suspension (pH 6.6) using a twin syringe pump (Harvard Apparatus). KOH solution was added
141 at 0.2 ± 0.05 ml/min and Fe(III) nitrate solution was added at 0.5 ± 0.05 ml/min. The pH of this
142 suspension was checked continuously, and the speed of addition was adjusted in order to avoid
143 strong decrease of pH values (pH remained ≥ 5.0). The amount of Fe was equivalent to two
144 times the cation exchange capacity (CEC) of illite (table 1), and KOH addition was stopped
145 when pH 7 was reached. The resulting suspension was then stirred for 1 h and the final
146 suspension was rinsed three times with ultrapure water to remove excess K^+, NO_3^- ions. The
147 aggregates were collected by centrifugation (15 min with 9000g), and freeze-dried. This method
148 was selected to avoid strong pH variations that might weather illite minerals or provoke the
149 precipitation of iron oxy-hydroxide in solution. This procedure is then slightly different from
150 those reported by (Liljestrand et al., 1992) and (Green-Pedersen and Pind, 2000). Furthermore,
151 the relatively low Fe concentration was selected not only to be closer to iron concentrations in
152 surface waters, but above all to favour iron oxy-hydroxide precipitation onto clay mineral
153 surfaces and to enhance homogeneous distribution of iron hydroxide particles on clay platelets.
154 *2.2.4. Supplementary model minerals*

Supplementary model minerals, goethite and calcite were also included in those investigations. Pure synthetic goethite (Sikovit 10E172) was purchased from BASF (Germany). The goethite particles are well-crystallized needles of an average size of 600 nm × 100 nm × 10 nm. (Prélot, 2001; Prélot et al., 2002). Calcite originated from Marocco (El Hammam mine, Meknes, Marocco), its purity was checked through XRD.

Ultra-pure water and American Chemical Society reagent-grade chemicals or better were used for all experiments. Glassware was soaked in 1 M HNO_3 for at least 12 h and rinsed three times prior to use.

2. 3. Methods for sample characterization

2.3.1. Electrophoretic mobility measurements

Electrophoretic mobility (EM) was measured with a zeta-phoremeter (Zetaphoremeter IV-CAD Instrumentations) equipped with a video interface via CCD camera. Measurements were carried out in a diluted suspension of SPM at constant ionic strength ($NaNO_3$, 0.01 mol/L), varying pH from 3 to 11 by adding acid (HCl) or base (NaOH) to the SPM suspension. The standard deviation provided with the EM values reports the distribution of particle velocities collected by the CCD camera, no bimodal distribution could be evidenced, and all the measurements on model and environmental particles provided a continuous distribution of electrophoretic mobilities.

2.3.2. Cation Exchange Capacity

Cation Exchange Capacity (CEC) was measured using the cobalt-hexamine trichloride ($Co(NH_3)_6Cl_3$) method (Ciesielski and Sterckeman, 1997; Orsini and Remy, 1976).

1.5 g of sample was dispersed and shaken during two hours at 30°C in 30 mL of cobalt-hexamine solution (16.6 $x10^{-3}$ mol L^{-1}). Samples were then centrifuged for one hour at 46,250

g. Supernatants were subsequently analysed on a UV–Visible spectrophotometer, using the intensity of the absorption band at 472 nm to evaluate residual concentration of cobalt-hexamine and derive the CEC of the solid. CEC was also estimated from the concentrations of released cations and concentrations of Na, K, Ca, Mg, Fe, Al and Si in supernatants were measured by atomic absorption, using a Perkin Elmer AA800 set-up (CRPG, Vandœuvre-lès-Nancy) to calculate CEC from the sum of exchanged cations. Measurements were always carried out in duplicate.

2.3.3. Nitrogen adsorption for textural characterization

Nitrogen adsorption-desorption isotherms at 77 K were recorded on a step-by-step automatic set-up (BET 2000). Prior to adsorption experiments, SPM and pure minerals (from 0.1 to 1 g) were outgassed at 50°C during 18 hours under a residual vacuum of 0.01 Pa (30°C for FeH and illite-FeH in order to not alter the iron (hydr)oxide (Hofmann et al., 2013). Specific Surface Areas (SSA) were determined from the Brunauer-Emmet-Teller (BET) equation (Brunauer et al., 1938) using 16.2 $Å^2$ as the cross-sectional area for nitrogen molecules. The De Boer method (or t –plot) was carried out to determine microporous volume and external surface area. Micropore filling happens at low and very low relative pressure values, and then includes the domain of the monolayer adsorption on external surface. To be able to distinguish adsorption onto external surface from adsorption into the micropores (pore size < 20Å), the experimental isotherm is compared to a reference curve obtained for a non-porous solid, with chemical features and energetic constant as close as possible to the studied matrix.

2.3.4. Zn adsorption isotherms, batch experiments

Adsorption isotherms were performed on SPM samples and pure minerals. They were obtained from batch experiments by varying Zn concentration in solution and using a constant solid/liquid ratio of 285 mg L^{-1}. This ratio was selected based on experimental feasibility, and

206 to be able to run spectroscopic measurements at Zn K-edge at the end of adsorption
207 experiments. The temperature was fixed at 25 °C, the pH of aqueous solution was fixed to pH
208 7.0 (±0.2) and the ionic strength was fixed either at 300 µS.cm^{-1} or 3000 µS.cm^{-1} using $NaNO_3$
209 solution in order to study the effect of conductivity on Zn adsorption. The mass of solid (m)
210 was fixed to 10 mg and added to a volume (V) of 35 mL of Zn solution of fixed concentration
211 ranging from 1 – 500 µmol L^{-1} in a 40 ml polyethylene centrifuge bottle. The mixture was then
212 shaken in a thermo stated (25°C) chamber overnight. The mixture was centrifuged at 19000
213 rpm during 20 min and the supernatant was filtered using 0.22 µm syringe filters. The solutions
214 were acidified, and initial and equilibrium Zn concentrations were determined by atomic
215 absorption, using a Perkin Elmer AA800 set-up (CRPG, Vandœuvre-lès-Nancy, France). The
216 amount of Zn adsorbed on solid (Qads) was obtained from the difference between the initial
217 (Ci) and the equilibrium (Ce) concentrations using the formula: $Qads = (Ci - Ce) * \frac{V}{m}$. The
218 solid fraction of each sample was collected, frozen, freeze-dried and pelletized prior to XAS
219 analysis. Each Zn adsorption experiment was performed using ten different Zn concentrations
220 referred to as Zni, *i* = 1 to 10. The Zn initial concentrations are for *i* = 1 to 10, 1 µmol L^{-1}, 2
221 µmol L^{-1}, 5 µmol L^{-1}, 10 µmol L^{-1}, 20 µmol L^{-1}, 50 µmol L^{-1}, 100 µmol L^{-1}, 200 µmol L^{-1} and
222 500 µmol L^{-1} respectively. The solid samples resulting from the Zn adsorption experiments are
223 referred to as *SPMname*Zni, *i* stating for the position on the Zn adsorption curve.
224 Supplementary Zn adsorption experiments were performed with higher ionic strength, *i.e.*,
225 electric conductivity was set to 3000 µS.cm^{-1} instead of 300 µS.cm^{-1}. A suffix *3k* was added to
226 the name of samples. Such batch experiments were performed for different SPM samples and
227 also for synthetic and pure mineral phases: illite, illite-FeH, and goethite. The end-members of
228 the adsorption isotherms, i.e., lowest and highest Zn loadings, were used as references for XAS
229 and were respectively referred as to Zn_{low}-Illite, Zn_{high}_Illite, Zn_{low}-Illite-FeH, Zn_{high}_Illite-
230 FeH, Zn_{high}_FeH and Zn_{high}_Goethite. In order to prepare supplementary Zn bearing phases as

reference samples for XAS spectroscopy, the same protocol was used with calcite. Those latter batch experiments provided two different samples for XAS, (i) Zn adsorbed onto calcite referred as to Znl_{ow}-Calcite, obtained with initial concentration in $Zn(NO_3)_2$ set at 10^{-6} mol L^{-1}, and displaying a Zn loading of 120 mg kg^{-1}; (ii) Zn coprecipitated onto calcite, referred as to Zn_{high}–Calcite, obtained with initial concentration in $Zn(NO_3)_2$ set at 5.10^{-4} mol L^{-1}, and displaying a Zn:Ca ratio of 0.16:1.

2.2.5 XAFS data collection and analysis

Most of the X-ray absorption spectra were collected at SAMBA beamline of the French National synchrotron facility SOLEIL located in Gif-sur-Yvette, France and a few complementary spectra (high Zn contents) were measured at the XAFS beamline from the Italian synchrotron facility ELETTRA (Trieste, Italy). The synchrotron ring was running at 2.75 GeV (SOLEIL) and at 2 GeV (ELETTRA) with an average current of 400 mA (SOLEIL) and 309 mA (ELETTRA). The X ray beam was monochromatized using a set of Si (220) on SAMBA beamline and Si (111) crystals on XAFS beamline. Experimental measurements were made at the Zn K-edge (9659 eV) and XAS spectra were collected in fluorescence detection mode using a CANBERRA 36 elements Ge detector on SAMBA and in transmission mode on XAFS beamline at Elettra. For all synchrotron sessions, the samples were prepared as pellets with at least 30 % of cellulose to increase the cohesive character of the pellet. The pellets were placed at 45° angle with respect to the incident beam for fluorescence and at 90° for transmission. All the spectra were collected using a cryostat chamber filled with liquid nitrogen at a temperature close to 77 K or -192 °C. Such a low temperature was sufficient to minimize thermal dampening of the EXAFS signal, and to slow down potential beam damage due to the presence of natural organic matter in the environmental samples. Between 4 and 6 scans were collected per sample to improve the signal to noise ratio.

Data extraction was performed using Athena software (Newville, 2001; Ravel and Newville, 2005). In order to calibrate energy for each Zn edge individual spectrum, a reference spectrum was obtained from a Zn foil set behind ionization chamber for transmitted beam. The first inflection point (zero on the second derivative) of the absorption edge was systematically set at 9659 eV for Zn foil spectra. For every sample spectrum, E_0 was set at the maximum of the first derivative of the absorption edge. k^3-weighted EXAFS were obtained from the background-subtracted and normalized spectra. Linear combination fitting (LCF) was performed on XANES and EXAFS regions of XAS spectra using ATHENA program (Isaure et al., 2002; Manceau et al., 1996). References were selected on the basis of SPM characterization and mineral phases identified (Le Meur et al., 2016).

For XANES, LCF fitting samples and reference spectra were all normalized in the same energy domain [20, 150] after E0. Fitting was performed on a restrained energy domain, -20 +120 around E_0, with a maximum number of components set to 3 and the sum of contributions forced to be equal to 1. Fitting solution was judged by the lowest R_x factor ($R_x = \sum_n(\mu_{exp} - \mu_{fit})^2/(\mu_{exp})^2$) and the number of components was increased only if it resulted in a consistent decrease of R_x (10%). The fitting solution was selected not only from the lowest residual component but also from visual appreciation and in particular we took into account the good reproduction of spectral features in the edge area, including the splitting of the edge when it was obvious. For EXAFS region, E_0 was set at the same value for all spectra in order to calculate $\chi(k)$ oscillations in the same k range. Fitting was performed on 3-11 $Å^{-1}$ k range with 4 components as a maximum. Quality of fit was checked with the fitting factor R_e ($Re = \sum_n(k^3\chi_{exp} - k^3\chi_{fit})^2/(k^3\chi_{exp})^2$), but also with qualitative appreciation on Fourier transforms (magnitude and imaginary parts).

We considered that those LCF results provided fractions of individual Zn bearing phases with a precision of about 10%. Limits and discussion about this fitting method have been previously

281 reported (Isaure et al. 2002). Shell-by-shell fitting was performed using the Artemis routine
282 from the IFEFFiT software (Newville, 2001; Ravel and Newville, 2005). The amplitude
283 reduction factor (S_0^2) was fixed at 0.7 for all shells. A good fit was determined on the basis of
284 the minimum residual error R_e, calculated with the same formulas for LCF.
285 Beside the reference samples already mentioned, additional reference spectra were obtained
286 from Zn-citrate and Zn-oxalate solutions (in fluorescence mode using a solution holder), from
287 a Zn-rich trioctahedral smectite, sauconite, provided by Stephan Kaufhold (Kaufhold et al.,
288 2015), and from other reference minerals: zincite, a double layer hydroxide Zn-HDL provided
289 by V. Briois (Carvalho et al., 2013; Roussel et al., 2001), amorphous zinc sulphide, wurztite
290 (ZnS), sphalerite (ZnS), a silicate, willemite (Zn_2SiO_4), and two spinels, gahnite ($ZnAl_2O_4$) and
291 franklinite ($ZnFe_2O_4$)) supplied by the French National Museum of Natural History (Paris,
292 France). The XANES and EXAFS data collected at Zn K-edge can be found in Appendix C
293 (https://doi.org/10.24396/ORDAR-26).

294

295 **3. RESULTS**

296 **3.1 Surface Properties of SPM samples and comparison to model particles.**

297 *3.1.1 Electrophoretic mobility (EM) and Cationic Exchange Capacity (CEC)*
298 Figure 1 shows the electrophoretic mobility (EM) curves obtained for the different model
299 particles suspended in aqueous solution ($NaNO_3$ 0.01 mol/L, pH adjusted from 3 to 11). The
300 illite particles display a negative EM curve for all the different pH values.
301 Those results were similar for both size fractions of illite and are close to those previously
302 determined on purified illite (Sondi et al., 1996). EM curve is dominated by the contribution of
303 the structural and thus permanent charge of illite particles, beside the variable surface charge
304 due to amphoteric edges. In comparison with other clay minerals, EM of illite particles tends
305 to show slight variations with pH, going towards less negative values in the acidic pH range [2

306 to 6] and towards more negative values for basic values of pH. This indicates a relatively large
307 fraction of amphoteric edges, but not to the extent of reaching positive EM in the conditions of
308 the measurements.
309 Although illite displays a relatively high density of charge, the contribution of variable charge
310 is enhanced by the size and shape of particles, and also the stage of aggregation, itself influenced
311 by the density of layer charge and location in the layer (Thomas et al., 1999). EM measured for
312 the iron oxyhydroxide, ferrihydrite, did not display the same trend as amphoteric surface sites
313 mainly govern it. The mixed compound illite-FeH displays similar results to that of illite,
314 suggesting that the charge of the mixed particles is close to that of the pristine illite, and that
315 aggregation state is rather close to that of pristine illite. However, the presence of iron oxy-
316 hydroxide coatings is unravelled by a slight modification of mobility at pH below 6. The low
317 extent of standard deviation also suggests a relative homogeneity of the mixed minerals.
318 Electrophoretic mobility was measured for distinct SPM samples, and two curves are presented
319 on Figure 1 (other curves are presented as supplementary material). For both samples the EM
320 is negative on the whole pH range suggesting the strong contribution of permanent negative
321 charge, such as illite, directly related to the mineralogical composition of SPM, mainly
322 constituted of clay minerals (Le Meur et al., 2016). In agreement with this assumption, the
323 sample FRO-Jul13, relatively depleted in clay minerals, displays a less negative electrophoretic
324 mobility than the sample FRO-Dec12. However, considering the range of values, as well as the
325 associated standard deviations, one can consider that those two SPM samples are rather close
326 in terms of electrophoretic mobility. Moreover, the standard deviations (see material and
327 methods part for their meaning), evidence that those samples are relatively disperse and
328 heterogeneous, certainly constituted of particles with different electrophoretic behaviour. When
329 comparing those SPM samples with the illite mineral (Figure 1), the presence of clay minerals
330 or negatively charged minerals is confirmed but their nature and/or shape might vary

consistently, resulting in a relatively more pronounced shift towards less negative values at low pH conditions. This difference of EM between SPM and illite can be due to different factors: the presence of clay minerals with low density of charge (kaolinite, montmorillonite, chlorite) and also the aggregation stage, reinforced by the presence of hydroxide coatings and organic matter (Chorom and Rengasamy, 1995; Thomas et al., 1999; Zhuang and Yu, 2002).

The cationic exchange capacities obtained for the different SPM samples are presented in Table 1. They are in the same range of order, and slightly higher than the CEC measured for the reference illite; these higher values can be explained by the presence of montmorillonite layers that are commonly displaying higher CEC values than illite minerals, and/or by the cation exchange capacity of organic matter (Parfitt et al., 1995). For FRO samples, we could not really evidence a relation between the CEC value and the organic matter content of SPM.

3.1.2. Textural properties

The specific surface areas (SSA) were measured for the different synthetized particles and are presented in the Table 1. The SSA is the highest for the FeH (218 m^2 g^{-1}). The illite displays a lower SSA (155 m^2 g^{-1}) and the illite-FeH sample presents a lower SSA of 124 m^2 g^{-1}, suggesting a reduction of accessible surface due to the presence of Fe-precipitates. The SSA was also measured for natural river SPM samples. SSA ranged between 6 and 37 m^2 g^{-1} and we could evidence an anti-correlation between these values and the organic matter content determined by thermogravimetric analyses (Le Meur et al., 2017). This relationship is also consistent with the increase of fine particles occurring with the increase of regime flow (in the range of these investigations, see Le Meur et al. 2016).

Then the influence of organic matter on textural properties of river SPM can be seen as a double effect, increasing the mean particle size through enhanced flocculation, and decreasing the specific surface area through the lower accessibility of external sites, at least for nitrogen

molecules. Based on nitrogen adsorption, none of the river samples displays a significant equivalent microporous surface area (always ≤ 1 m^2 g^{-1}) while the model particles, except goethite, show a microporous surface area ranging between 28 and 47 m^2 g^{-1}.

3.2. Zn adsorption isotherms: batch experiments as a function of Zn concentration

3.2.1. Zn adsorption on lab-controlled mineral phases

These experiments were all performed in the same conditions of pH, ionic strength and solid:liquid ratio for model and environmental solid samples. A comparison of Zn(II) uptake on Illite, FeH, Goethite and Illite-FeH is shown on Figure 2A.

As expected, and as previously reported (Bradbury and Baeyens, 1999; Lee et al., 2004; Nachtegaal and Sparks, 2004; Trivedi et al., 2001b, 2001a; Waychunas et al., 2003), these experiments confirm the relatively high affinity of Zn for mineral surfaces, with a strong adsorption at Zn concentrations between 0.1 and 1 micromole L^{-1}. Maximal adsorption values are 57 mmole kg^{-1} for FeH, 58 mmole kg^{-1} for goethite, 89 mmole kg^{-1} for illite whereas illite-FeH displays intermediate adsorption capacities (75 mmol kg^{-1}). For Zn concentrations higher than 0.1 mmol L^{-1}, the curve shapes suggest (i) adsorption on less energetic sites forming loose surface complexes with long-distance forces, or (ii) slow diffusion in the mineral or (iii) precipitation. In the case of illite-FeH, textural properties were similar to those of illite, and this sample shows slightly lower maximal adsorption values than illite, certainly due to the slight decrease of highly energetic sites for the adsorption of Zn (Nachtegaal and Sparks, 2004)

3.4.2 Zn adsorption on River SPM

Adsorption isotherms were also performed for SPM samples (Figure 2B and 2C). None of the sorption isotherms can be interpreted with the Langmuir model (Benjamin and Leckie, 1981). Such an observation was expected due to the heterogeneous character of SPM composition and the high diversity of surface groups. The SPM adsorption isotherms show a relatively strong

adsorption for low Zn concentrations (Figure 2B) suggesting the presence of high affinity sites. Most of the SPM samples display Zn adsorption isotherms with a similar shape, except two of them, one collected from a highly impacted tributary (FLO) and one collected at the most downstream station (THI). Those two samples are rather different in terms of element concentrations, mineralogy and organic matter content. They both display high iron and organic matter contents that might explain their relatively stronger adsorption capacity (Le Meur et al. 2015). Maximal adsorbed Zn values were obtained for FLO sample (547 mmol kg^{-1}). Since those SPM were shown to be particularly rich in organic matter and iron oxyhydroxides, but rather depleted in clay minerals, it can be assumed that the strong adsorption capacity of this SPM sample was certainly due to organic matter and/or iron oxyhydroxide binding. The samples FRO-Dec12, FRO-Jul13 and FRO-Jun13 show strong similarities in terms of adsorption capacities and thus isotherm curve shape. However, FRO-Dec12 sample displays higher adsorption capacities at the beginning of the isotherm, suggesting that those river particles display a higher number of highly energetic adsorption sites. This difference of behaviour towards Zn might be due to the amount of clay minerals, higher for FRO-Dec12. Adsorption mechanisms cannot be derived from these simple batch experiments, and supplementary investigations as a function of pH, time, solid:liquid ratio, ionic strength, nature of the ions in solution (Na^+ vs Ca^{2+} for instance) would certainly provide clearer assumptions. For that purpose, XAS measurements were performed to evidence the adsorption mechanisms of Zn on those natural particles. An increase in ionic strength (graph C on Figure 2) did not modify the shape of the sorption curves but the amount of adsorbed Zn is reduced for the high Zn concentrations, certainly due to the screening of the particle charge by major ions.

3.5 Zn binding mode on SPM and model mineral phases

3.5.1 XANES spectra obtained for Zn adsorbed onto model phases

407 XANES spectra obtained after Zn adsorption on synthetic and purified mineral phases are
408 presented on Figure 3. XANES features such as the position and shape of the edge are
409 informative about Zn coordination and binding mode with the mineral surfaces (Waychunas et
410 al., 2003).
411 On Figure 3, the XANES spectrum of Zn_{high}-FeH (curve h), displays two well-defined peaks at
412 9665.5 and 9669 eV. The absorption edge position suggests that Zn is partially in tetrahedral
413 coordination. It was previously shown that Zn is adsorbed on ferrihydrite as a tetrahedral
414 bidentate corner-sharing complex (Waychunas et al., 2003, 2002), except for very high Zn
415 loadings, for which most of Zn remains octahedrally coordinated as in solution.

416 Cismasu et al. (2013) recorded XANES for Zn adsorbed onto FeH and Al substituted FeH with
417 different surface coverages. They could evidence the same features as those shown on Figure
418 3. However, they showed a third supplementary peak at 9675 eV that decreased in intensity
419 with increasing Zn coverage, not detected in our study. They concluded as Waychunas et al
420 (2003) that Zn was predominantly tetrahedrally coordinated when adsorbed onto ferrihydrite
421 and onto Al- or Si-substituted ferrihydrites.
422 XANES spectrum for illite (Figure 3, curve b) displays two well-defined peaks at 9665.5 and
423 9669 eV respectively, but with inverted intensities in comparison with that of Zn_{high}-FeH.
424 Furthermore, a well-defined shoulder can be observed at 9673 eV. The On the opposite, for
425 higher Zn loadings, the XANES spectrum of Zn_{high}-illite (Figure 3, curve e) displays only one
426 major broad peak at 9669 eV, suggesting that Zn is mainly in octahedral coordination, and with
427 no well-defined distribution of oxygen in the first coordination shell. Those spectra were also
428 compared to that of pristine illite that contains zinc in its crystal lattice (Figure 3, left graph,
429 curve b, Zn-crystal-illite, Zn content 171 $mg.kg^{-1}$) and to that of sauconite (Figure 3 left graph,
430 curve a), a zinc-rich smectite, in which Zn occupies most of the octahedral layer (trioctahedral
431 layer). For the three spectra related to sauconite, illite and Zn_{low}-illite (Figure 3, curves a, b and

c), respectively, three components at 9665.5, 9669 and 9673 eV are noticeable with distinct intensity ratios. Clearly, even if Zn is assumed to keep an octahedral coordination, XANES features are relatively complex for illite and sauconite samples, and as far as we know, no theoretical model was reported to explain the different features in the edge region. The predominance of the absorption contribution at 9669 eV for the spectrum of sauconite can be explained by the relative homogeneity of local environment around Zn in that clay mineral. Indeed, since this smectite is trioctahedral (no vacant site in the octahedral layer), most Zn atoms have an identical local environment, with a similar distribution of neighbouring atoms (distance and nature). The post-edge features (at energies higher than 9680 eV) are common for both illite and sauconite, with a well-marked peak at 9686 eV and a split first oscillation with two maxima around 9710 and 9720 eV. Those post-edge features are close to those reported for Zn adsorbed onto amorphous alumina-silicate and Al_2O_3 (Miyazaki et al., 2003). The comparison between illite and sauconite XANES spectra suggests that short-range backscattering, due to the scattering of ejected electrons by the oxygen atoms of the first coordination shell, mainly influences the post-edge features. Beside this first observation, the edge features are not only influenced by the coordination, but they are also linked to long-distance scattering and evidence the existence of distinct octahedral sites within illite. No difference is observed between Zn adsorbed on illite and on illite/FeH (Figure 3, left graph, curves c and d and curves e and f), suggesting that the presence of iron oxyhydroxides on clay minerals does not modify Zn binding or that this modification is too weak to be detected by XAS. This observation concurs with the similarity of adsorption isotherm curves and confirms that illite surface sites control Zn adsorption for this compound. The two bottom spectra (i and j curves on left graph, Figure 3) correspond to the reference samples prepared from the aqueous adsorption of Zn onto calcite. Zn_{low}-calcite spectrum is relatively close in terms of general shape to the XANES spectrum reported for Zn adsorbed onto calcite (Elzinga and Reeder, 2002). The

457 spectrum of Zn_{high}-calcite displays some common features to that of hemimorphite (Elzinga and
458 Reeder, 2002) although this Zn bearing mineral was not included in our reference library, as
459 we did not expect well-crystallized Zn bearing phases in our set of SPM samples. Both spectra
460 show low intensity white line as well as a contribution at 9665.5 eV. Those two details suggest
461 that Zn atoms have partially or totally a tetrahedral coordination. This assumption will be
462 confirmed by the shell-by-shell fitting of EXAFS region (see following paragraphs, Table 3
463 and Figure 4).
464
465 *3.5.2. XANES spectra obtained for Zn adsorbed onto river SPM*
466 Zn K-edge XANES spectra were recorded for Moselle River SPM, before and after Zn
467 adsorption at different Zn concentrations (Figure 3, middle and right graphs). Two SPM
468 samples were selected on the basis of their organic matter content and mineralogy: FRO-Jul13
469 and FRO-Dec12. Initial SPM spectra show rather similar trends with two well-defined peaks at
470 9665.6 (± 0.2) eV and 9669 (± 0.2) eV for FRO-Jul13 and for FRO-Dec12.
471 However, some differences can be noticed from the two spectra and in particular in the post-
472 edge region. FRO-Dec12 spectrum displays a sharper feature at 9687 eV and the first oscillation
473 is split with two maxima at 9709 and 9723 eV. The post-edge features noticed on the spectrum
474 of FRO-Dec12 suggest a contribution of Zn inserted in phyllosilicate structure as the latter split
475 was also observed for sauconite and illite (Figure 3, curves a and b).
476 Linear combination fitting of those two XANES spectra suggested that Zn is predominantly
477 inserted in the structure of dioctahedral clay for SPM sample FRO-Dec12, whereas the SPM
478 sample FRO-Jul13 displays a relatively strong contribution of Zn associated with iron-
479 oxyhydroxides (Table 2). Upon Zn adsorption, the features on SPM samples FRO-Jul13 are
480 progressively disappearing with the increase of Zn loading (Figure 3, middle graph curves a to
481 f). For experiments conducted with higher conductivity (curves g to i), the spectra appear
482 smoothed with one main feature in the edge region, centred around 9669 eV. With increase of

Zn surface coverage, the 9665.6 eV peak, assigned to Zn inserted in octahedral layer of phyllosilicates, decreases in both cases and the general shape of XANES gets smoother and close to the spectra obtained for high Zn surface coverage of illite and illite-FeH. With increasing Zn loading, the mineral surface groups binding Zn do not influence anymore the coordination sphere of Zn, and the distribution of water molecules around Zn is not constrained by the mineral surface anymore.

For Zn adsorbed onto FRO-Dec12, the XANES fitting evidenced the contribution of Zn adsorbed onto calcite while the signal of Zn adsorbed onto FRO-Jul13 is predominated by Zn adsorbed onto illite and iron hydroxide (Table 2). The role of organic matter was not readily evidenced with these spectroscopic data.

3.5.3. Evidence of Zn binding mode on model minerals and SPM, interpretation of EXAFS oscillations

Association mode of Zn on model minerals and natural SPM was also investigated through the mathematical analysis of EXAFS oscillations, using both linear combination fitting and shell-by-shell fitting. EXAFS oscillations are supposed to report the spatial distribution of atoms around Zn, and in the case of complex systems, LCF using well-known Zn bearing minerals is preferred (Catalano et al., 2012; Le Pape et al., 2014; Luo et al., 2011; Scheinost et al., 2002). Figure 5 presents the main reference EXAFS curves used for such linear combinations.

Beside Zn oxides and sulphides, the solids resulting from Zn adsorption on reference minerals (illite, calcite, goethite and ferrihydrite) were used as standard samples for the reproduction of SPM EXAFS curves. Zincite EXAFS curve displays relatively high amplitude in oscillations, due to the high crystallinity of zincite. Indeed, zincite is the only crystalline sample among the references presented on Figure 4.

Due to the predominance of clay minerals in natural SPM samples, and in particular illite minerals, two natural Zn bearing phyllosilicates were used as references for Zn incorporated in

509 phyllosilicate structure. EXAFS oscillations from a zinciferous smectite (sauconite, curve b on
510 Figure 5) display a first double-bounced oscillation with maxima at 3.6 and 3.9 $Å^{-1}$ and a second
511 oscillation split into two peaks at 5.1 and 5.8 $Å^{-1}$. The third curve (curve c) was obtained from
512 size-fractionated illite du Puy, a clay mineral that naturally contains Zn (about 220 mg kg^{-1}).
513 EXAFS oscillations display noticeable features that can be related to those previously described
514 for zinciferous smectite: a first oscillation double-bounced at 3.5 and 4 $Å^{-1}$ and a second
515 oscillation centred at 5.9 $Å^{-1}$ that can be described as a triple-bounced oscillation, displaying
516 two shoulders at 5.2 and 6.4 $Å^{-1}$. Those features on illite signal are typical of Zn bearing
517 phyllosilicates with relatively low Zn content (trace level) and were previously reported,
518 structurally interpreted and modelled (Churakov and Dähn, 2012; Dähn et al., 2011; Jacquat et
519 al., 2008; Juillot et al., 2006; Schlegel et al., 2001). With low Zn adsorption, Zn_{low}-illite EXAFS
520 signal (curves c and d respectively on Figure 4) presents similar features but there is an
521 attenuation of the scattering contribution at 3.5 $Å^{-1}$ and the shoulder at 5.9 $Å^{-1}$ is smoothed. This
522 evolution of EXAFS signal with Zn adsorption is identical or strongly similar to that observed
523 for montmorillonites (STx and Milos) (Dähn et al., 2011). This evolution of EXAFS signal
524 strongly suggests that for Zn_{low}-illite, Zn is adsorbed onto edge sites in the continuity of the
525 octahedral sheet. For higher Zn loading (Zn_{high}-illite, curve e), EXAFS signal is different, with
526 a smoothed signal suggesting the predominance of outer-sphere complexes and the adsorption
527 of Zn on weak sites, certainly including basal sites where exchangeable cations are positioned.
528 Figure 4 also displays the EXAFS signals obtained for Zn adsorbed onto calcite (Figure 5 curves
529 f and g). Zn adsorption onto carbonates was studied through two end-member samples, obtained
530 with the lowest and highest initial Zn concentrations in solution, and respectively referred to as
531 Zn_{low}-Calcite and Zn_{high}-Calcite. The Zn_{low}-Calcite EXAFS signal is marked by the splitting of
532 the first oscillation at 4 $Å^{-1}$ and by the presence of a low maximum at 7 $Å^{-1}$. This EXAFS curve
533 can be compared to those of smithsonite ($ZnCO_3$) or Zn substituted calcite (Jacquat et al., 2008),

534 although in our case the Zn:Ca atomic ratio is about ten times lower than that reported by
535 Jacquat et al (2008) for their Zn substituted calcite. Furthermore, in our study, XAS spectra
536 were recorded at low temperature (using a liquid N_2 cryostat), while those reported by Jacquat
537 et al. were obtained at ambient temperature. This different experimental parameter is known to
538 induce differences in the global aspect of oscillations in the high *k* range, so the comparison
539 between the current EXAFS signals and those reported by Jacquat et al is rather limited. The
540 Zn_{high}-Calcite signal is very similar to that standing for Zn adsorbed onto calcite (Elzinga et al.,
541 2006; Elzinga and Reeder, 2002; Jacquat et al., 2009).
542 For references with high Zn loadings (Figure 5 curves e, g and h), the oscillations are dominated
543 by the backscattering of oxygen atoms from the first coordination sphere, as already suggested
544 by XANES spectra. Furthermore, shell by shell fitting confirmed the predominance of oxygen
545 atoms scattering (Appendix E). Zn_{high}-FeH curve is essentially due to the backscattering signal
546 of oxygen atoms from the first coordination sphere, in both tetrahedral (Zn-O 1.96 Å) and
547 octahedral (Zn-O 2.13 Å) configurations and only a minor contribution of Fe atoms as second
548 neighbours could be evidenced. For Zn_{high}-calcite and Zn_{high}-illite, the same trend was observed,
549 suggesting that Zn was bound as an outer-sphere adsorption complex or inner-sphere adsorption
550 complex with weak backscattering from atoms of the mineral surface.
551
552 *3.5.3. Evidence of Zn binding mode in SPM before and after Zn batch experiments,*
553 *interpretation of EXAFS oscillations*
554 Figures 5 and 6 present the EXAFS oscillations obtained for FRO-Jul13 and FRO-Dec12 before
555 and after Zn adsorption, as well as the corresponding Fourier Transforms. In both cases there
556 is a clear modification of EXAFS signals with zinc adsorption. Signal modifications due to Zn
557 adsorption are clear for both SPM samples even if Zn speciation in SPM is initially different.
558 The Zn signal evolves in different ways for these two SPM samples. EXAFS data on original
559 SPM samples (Figure 5 and 6, curves a) display a relatively high noise level in the high k range,

560 certainly due to a combination of the amorphous character of SPM and the low Zn content (260-
561 300 mg kg^{-1}). The FRO-Dec12 sample shows higher splitting of the first oscillation than the
562 FRO-Jul13 sample, certainly due to the predominance of Zn inserted in phyllosilicate structure
563 for this sample. Indeed, LCF suggests the predominant contribution of Zn_{low}-illite (73 %) for
564 FRO-Dec12. FRO-Jul13 was evaluated by LCF as the contribution of three different Zn bearing
565 phases, Zn_{low}-illite (about 50%), Zn_{high}-FeH and zincite (about 25% each) (Table 3, Figure 5).
566 Those results are consistent with the mineralogical composition of the two SPM samples, FRO-
567 Dec12 being mainly constituted of clay minerals (Figure 7 Table 3).
568 After Zn adsorption, the increase of Zn loading on FRO-Jul13 (Figure 5 curves b to f, from the
569 top to the bottom) induces the diminution and disappearing of the features assigned to second
570 neighbours backscattering, at 7 $Å^{-1}$ and 9 $Å^{-1}$. For high Zn loading, the EXAFS signal is
571 essentially assigned to the first shell of neighbouring atoms, i.e. oxygen atoms of the
572 coordination sphere. However, for FRO-Dec12 sample (Figure 6), the increase of Zn loading
573 results in the splitting of the third oscillation initially centred at 7.7 $Å^{-1}$ that becomes a double
574 hill at 7.3 and 8 $Å^{-1}$. On Fourier Transform curves, a contribution in the 2nd or 3rd coordination
575 sphere concomitantly appears (Figure 6, right graph R = 3.3 Å). In that case, we concluded that
576 for FRO-Dec12 sample, the association mode of Zn was not restrained to outer sphere complex
577 but implies also the formation of bindings with the surface of river particles.
578 Shell by shell fitting using theoretical backscattering signal was also performed for those two
579 initial SPM samples (Figures 7 and 8, Tables 4 and 5). The theoretical fitting shows that oxygen
580 atoms in octahedral coordination compose the first coordination shell of Zn in sample FRO-
581 Dec12 (Zn-O 2.09 Å). For FRO-Jul13, the theoretical fitting evidences the predominance of
582 oxygen in the first coordination sphere of Zn but the fit also suggests the contribution of S
583 backscattering with Zn-S distances at 2.32 Å and Zn backscattering with Zn-Zn distances at
584 3.18 and 4.15 Å (Table 4).

585 The binding of Zn onto SPM samples is fitted by the signal of Zn adsorbed onto model minerals
586 illite, calcite and ferrihydrite (Table 3). With the increase of Zn loading, the contribution of
587 Zn_{high}illite increases for both SPM samples, and appears predominant for the highest Zn
588 loading, FRO-Jul13 Zn10 and FRO-Dec12 Zn10. Globally, linear combination fitting of
589 EXAFS oscillations provides results like those obtained on XANES region.
590 Shell-by-shell fitting revealed Zn surface complexation (Figure 7 and 8 Tables 4 and 5). Beside
591 the first coordination layer, constituted of six oxygen atoms in octahedral symmetry with a
592 bonding distance Zn-O of 2 Å, the second shell fitting shows the presence of Zn-Zn distances
593 at 3.2 Å.
594
595 **4. DISCUSSION**

596 **4.1. Moselle River SPM reactivity - Comparison with other studies**

597 The reactivity of natural particles including their complex capacity was investigated in several
598 studies (Borgnino et al., 2010; Ferreira et al., 1997; Lead et al., 1999; Minaberry and Gordillo,
599 2010, 2007) targeting riverine, estuarine suspended particles or soil and sediments constituents.
600 In numerous studies, clay minerals were shown to play a major role in the complexation of
601 metals. As mentioned by Minaberry and Gordillo, the nature and proportions of clay minerals
602 certainly vary from one river to another, and it is crucial to consider the mineralogy of the
603 adsorptive constituents before comparing the SPM from one river to another. In the case of the
604 Moselle River, we could show that the contribution of clay minerals to SPM can also vary with
605 hydrological conditions in the case of urbanized watershed (Le Meur et al., 2016) and finally
606 we evidenced that the Zn adsorption isotherms differ slightly from one SPM sample to another.
607 Indeed, different SPM samples were tested, displaying different clay mineral contents, different
608 organic matter contents and different iron oxyhydroxide contents. However, excepted FLO-
609 Oct12, the shape of Zn adsorption isotherms is rather similar, suggesting that the binding sites
610 involved in the complexation of Zn are globally the same. Bibby and Webster-Brown (2006)

611 also performed Zn batch isotherms on river SPM. They observed almost no difference in terms
612 of Zn adsorption between the different SPM investigated (urban versus non-urban SPM and
613 regime flow, seasonal variations) despite some differences in composition. The Zn
614 concentration used for their study was set to 500 µg L^{-1} (about 7.7 µmol L^{-1}), close to the third
615 point of our adsorption experiments (Zn3, 5 µmol L^{-1}). Zn adsorption was modelled assuming
616 that hydrous ferric oxide (HFO) was the main adsorbing mineral surface, but the authors
617 evidenced some discrepancies between the adsorption model and their experiments, underlining
618 the complexity of SPM composition and the diversity of functional groups that might bind Zn.
619 The SPM sample FLO-Oct12 states as the Fe and organic matter richest sample, and we could
620 evidence that its capacity to sorb Zn is far much higher than that of other samples (Figure 2).
621 In line with the previous sentences, Sipos et al. evidenced the influence of Fe content on the
622 adsorption of four metals including Zn. Indeed, the higher the Fe content, the higher the
623 adsorption capacity of natural particles. They also showed that the presence of Fe particles or
624 Fe coatings on clay mineral surfaces affect the metal adsorption capacity (Sipos et al., 2018,
625 2008). However, the Zn concentration selected for their adsorption experiments was set to 10
626 mmol L^{-1}, i.e., from twenty times to one hundred times higher than the Zn concentrations
627 selected for our study. In order to test the influence of the presence of iron on Zn adsorption,
628 Fe-coated illite was prepared, through a specific procedure, hydrolysing iron solution in the
629 presence of illite particles. Although the presence of iron particles on illite surfaces was
630 confirmed with TEM (data not shown in this publication, see Le Meur PhD manuscript (Le
631 Meur, 2016)), the presence of these iron oxyhydroxide particles did not affect the binding mode
632 of Zn, of if it was, we could not detect it.
633
634 **4.2. Zn speciation in SPM - Comparison with other studies**
635 EXAFS results show a rather complex Zn speciation in SPM from the Moselle River, and this
636 speciation varies with the regime flow. Few studies report Zn speciation on SPM from rivers.

637 Le Pape et al. (2014) studied Zn speciation in SPM from the Orge River, a tributary of the Seine
638 River, located in a densely urbanized catchment. Bonnot et al. (2016) also studied three sub-
639 catchments of the Seine watershed. In both publications, Zn was reported to be associated with
640 ferrihydrite, calcite and clay, reported as geogenic minerals, and amorphous sulphides, assumed
641 to appear through the mobilization of anoxic sediments of the riverbed or urban sewer system.
642 They also reported a clear difference in speciation between low flow and high flow regime. In
643 the Orge River, during high flow regime, for urbanized and non-urbanized stations, Zn was
644 shown to be mainly adsorbed onto geogenic particles (calcite, clay) suggesting soil runoff and
645 suggesting lithogenic source of Zn. During low flow regime, Le Pape et al 2014 showed that
646 Zn was associated with amorphous SiO_2 and phytate, suggesting the presence of Zn adsorbed
647 to diatoms as diatoms can sorb trace metals in such pH conditions. The sample FRO-Jul13 was
648 also characterized by the presence of diatoms in higher content that FRO-Dec12. However, no
649 Zn-diatom association could be deduced from the EXAFS data.
650 Voegelin et al. (2002) worked on Zn adsorption using soil columns and evidenced the formation
651 of Zn-Al double layer hydroxide (Zn-Al LDH). This Zn species was evidenced from XAS data
652 and more precisely from the presence of a multiple scattering feature at 8 $Å^{-1}$ on EXAFS curves
653 and multiple scattering peaks at 6 Å on Fourier Transforms. Such features were absent from
654 our EXAFS and Fourier Transform curves and the hypothetical formation of Zn-Al LDH was
655 discarded (Voegelin et al., 2002).
656
657 4.3. **Deciphering Zn binding mode in complex samples**
658 SPM samples are complex systems, constituted of environmental particles of different kinds,
659 displaying multiple mineral phases, biological and organic matter. In this work we have tried
660 to approach the binding mode of Zn with environmental particles combining direct and indirect
661 methods. First, the comparison of SPM properties and Zn adsorption isotherms suggested some
662 correlations between the composition of SPM and their reactivity. Indeed, the presence of

663 organic matter (FLO-Oct12) was evidenced for one organic-rich sample and we could assume
664 that Zn was mainly bound to organic matter in that particular case. The two SPM samples FRO-
665 Jul13 and FRO-Dec12 were distinct in terms of organic matter content and mineralogy. The
666 latter was richer in inorganic components, was sampled during a flood event (see table 1) and
667 can be considered as a real detrital sample. Beside the composition, the characterization of these
668 two samples did not evidence clear distinction in terms of external properties. EM
669 measurements and Zn batch adsorption experiments evidenced similar surface properties. XAS
670 finally pointed out clear differences in the association mode of Zn. Such findings finally
671 highlight the fact that the external properties are globally driven by the major components of
672 the SPM samples (organic matter, clay mineralogy, iron content) but Zn adsorption reflected
673 the presence of specific adsorption sites that are not readily related to a precise organic or
674 mineral phase. XAS investigation of Zn adsorbed onto FRO-Dec12 evidenced the formation of
675 inner sphere complexes.
676
677 The complexity of natural material makes the XAS data difficult to fit. Thus, the interpretation
678 of XAS data for Zn adsorbed onto SPM is not unique. Linear combination fitting is one way to
679 simplify the interpretation, provided that the reference library of XAS standard spectra is
680 sufficiently exhaustive or relevant so that the spectra can be fitted with consistency and
681 robustness.
682 However, the gap between reference standards used for LCF and environmental particles is still
683 large and the strategy of combining several signals from pure references to mimic that of a
684 complex mixture presents some limitations. Indeed, such a fitting procedure cannot reproduce
685 the diversity of the chemical status of Zn in such samples. LCF procedure is commonly
686 constrained by a preliminary PCA in order to estimate the number of components to use to fit
687 XAFS data. Furthermore, the references to be used for fitting are selected through a target

688 transformation (Beauchemin et al., 2002). Searching for the main binding mode of Zn adsorbed
689 onto SPM can be considered as a way to probe the reactivity of SPM and evidence the main
690 association types that may form between the metal and the environmental particles.
691 In this work we have tried to compare model and environmental samples not only in terms of
692 Zn binding mode but also in terms of external properties such as electrophoretic mobility,
693 surface area, CEC. The complexity of environmental samples is difficult to reproduce or mimic
694 and selecting rather classical mineral phases can be seen as a first step.
695
696 **CONCLUSION**
697 The previous paragraphs presented the detailed characterization of natural river samples
698 including their external properties and their reactivity towards Zn, a commonly encountered
699 metallic pollutant in continental rivers. Several bulk techniques were used including
700 electrophoretic mobility, nitrogen adsorption experiments, batch zinc adsorption experiments
701 and X-ray absorption spectroscopy to unravel the zinc association mode and reactivity of
702 environmental particles. The bulk external properties of river samples could be related to their
703 contents in organic matter and clay mineral. Indeed, the presence of clay minerals enhanced the
704 adsorption capacity when Zn concentrations are below 1 micromole L^{-1} while the organic matter
705 tended to enhance the adsorption of this element for concentrations higher than 10 micromole
706 L^{-1}. However, surface properties (EM) and Zn adsorption were not completely predicted by
707 organic and clay mineral contents. Furthermore, spectroscopic investigations evidenced slightly
708 different binding modes for similar batch Zn adsorption results, revealing the complexity of
709 environmental particles and the difficulty to predict their reactivity on the basis of bulk
710 charaterization. This study also investigated the reactivity and association mode of Zn in lab-
711 controlled particles (illite, FeH, illite/FeH, calcite) and the pre-cited minerals were compared
712 with river particles. Zn adsorption capacity was definitely stronger for river particles at low and
713 high ranges of Zn concentrations, whatever the localization or hydrological conditions of

sampling. This second point evidenced also the difficulty to mimic environmental particles and reproduce their reactivity properties with pure mineral. thThese results revealed the usefulness of XANES and EXAFS investigation to probe Zn speciation in complex natural particles such as river SPM and to predict the binding mode of Zn, and finally its behavior and fate in continental waters.

AUTHOR CONTRIBUTION

Mathieu LE MEUR wrote the first draft of the paper and Emmanuelle MONTARGES-PELLETIER wrote the final version of the paper. All the authors reviewed the final version of the paper and contributed to data collection and results interpretation. In more details, Laurent MICHOT, Valerie BRIOIS and Hussein KANBAR specifically contributed to the acquisition of XAS data. Renaud GLEY participated to the river material sampling, to the characterization of natural and reference materials and performed the cationic exchange capacity measurements. Angelina RAZAFITIANAMAHARAVO performed the textural analysis and helped for their interpretation. Celine CAILLET contributed to the measurements of electrophoretic mobility and helped for the interpretation. Emmanuelle MONTARGES PELLETIER and Frederic VILLIERAS supervised this work and Emmanuelle MONTARGES PELLETIER oversaw funding acquisition.

ACKNOWLEDGMENTS

Region Lorraine (CPER ZAM), the French Ministry of Higher Education, Research and Innovation (PhD fellowship), and CNRS INEE (French eLTER), and the French National Agency for Research (ANR - project number ANR-14-CE01-0019) brought financial support to this work. We acknowledge SOLEIL for provision of synchrotron radiation and we would like to thank Emiliano FONDA and Andrea ZITOLO for assistance in using beamline SAMBA. We also acknowledge ELETTRA Synchrotron facility and thank Giuliana AQUILANTI and Luca OLIVI from XAFS beamline. The research leading to these results has been supported by the project CALIPSOplus under the Grant Agreement 730872 from the EU Framework

741 Programme for Research and Innovation HORIZON 2020. We also thank Sylvie MIGOT and
742 Jaafar GHANBAJA for the access to the Transmission Electron Microscope CM200 (Institut
743 Jean Lamour, University of Lorraine).

744

745 **APPENDICES and DATA**

746 Supplementary data can be downloaded from the French Data Repository Ordar.

747 A-Elemental composition of Moselle SPM samples https://doi.org/10.24396/ORDAR-62
748 B-Illite data, https://doi.org/10.24396/ORDAR-28
749 C-Zn XAS reference spectra, https://doi.org/10.24396/ORDAR-26
750 D-Electrophoretic mobility of river suspended materials.
751 E-Zn references, shell by shell fitting of EXAFS oscillations for Zn_{low}-calcite, Zn_{high}-calcite,
752 Zn_{high}-ferrihydrite, Zn_{low}-illite, Zn_{high}-illite.
753

754 **REFERENCES**

755 Beauchemin, S., Hesterberg, D., Beauchemin, M., 2002. Principal Component Analysis
756 Approach for Modeling Sulfur K-XANES Spectra of Humic Acids. Soil Sci. Soc. Am. J.
757 66, 83–91. doi:10.2136/sssaj2002.8300

758 Bengtsson, G., Picado, F., 2008. Mercury sorption to sediments: Dependence on grain size,
759 dissolved organic carbon, and suspended bacteria. Chemosphere 73, 526–531.
760 doi:10.1016/j.chemosphere.2008.06.017

761 Benjamin, M.M., Leckie, J.O., 1981. Competitive adsorption of Cd, Cu, Zn, and Pb on
762 amorphous iron oxyhydroxide. J. Colloid Interface Sci. 83, 410–419. doi:10.1016/0021-
763 9797(81)90337-4

764 Bibby, R.L., Webster-Brown, J.G., 2006. Trace metal adsorption onto urban stream suspended
765 particulate matter (Auckland region, New Zealand). Appl. Geochemistry 21, 1135–1151.
766 doi:10.1016/j.apgeochem.2006.03.014

767 Blachier, C., Jacquet, A., Mosquet, M., Michot, L., Baravian, C., 2014. Impact of clay mineral
768 particle morphology on the rheological properties of dispersions: A combined X-ray
769 scattering, transmission electronic microscopy and flow rheology study. Appl. Clay Sci.
770 87, 87–96. doi:10.1016/j.clay.2013.11.004

771 Borgnino, L., Garcia, M.G., del Hidalgo, M. V., Avena, M., De Pauli, C.P., Blesa, M.A.,
772 Depetris, P.J., 2010. Modeling the Acid–Base Surface Properties of Aquatic Sediments.
773 Aquat. Geochemistry 16, 279–291. doi:10.1007/s10498-009-9079-y

774 Bradbury, M.H., Baeyens, B., 1999. Modelling the sorption of Zn and Ni on Ca-
775 montmorillonite. Geochim. Cosmochim. Acta 63, 325–336. doi:10.1016/S0016-
776 7037(98)00281-6

777 Brunauer, S., Emmett, P.H., Teller, E., 1938. Adsorption of Gases in Multimolecular Layers. J.
778 Am. Chem. Soc. 60, 309–319. doi:10.1021/ja01269a023

779 Buyang, S., Yi, Q., Cui, H., Wan, K., Zhang, S., 2019. Distribution and adsorption of metals
780 on different particle size fractions of sediments in a hydrodynamically disturbed canal.
781 Sci. Total Environ. 670, 654–661. doi:10.1016/j.scitotenv.2019.03.276
782 Carvalho, H.W.P., Pulcinelli, S.H., Santilli, C. V., Leroux, F., Meneau, F., Briois, V., 2013.
783 XAS/WAXS Time-Resolved Phase Speciation of Chlorine LDH Thermal Transformation:
784 Emerging Roles of Isovalent Metal Substitution. Chem. Mater. 25, 2855–2867.
785 doi:10.1021/cm401352t
786 Catalano, J.G., Huhmann, B.L., Luo, Y., Mitnick, E.H., Slavney, A., Giammar, D.E., 2012.
787 Metal release and speciation changes during wet aging of coal fly ashes. Environ. Sci.
788 Technol. 46, 11804–11812. doi:10.1021/es302807b
789 Chen, J., Huang, D.J., Tanaka, A., Chang, C.F., Chung, S.C., Wu, W.B., Chen, C.T., 2004.
790 Magnetic circular dichroism in Fe 2p resonant photoemission of magnetite. Phys. Rev. B
791 69, 85107. doi:10.1103/PhysRevB.69.085107
792 Chorom, M., Rengasamy, P., 1995. Dispersion and zeta potential of pure clays as related to net
793 particle charge under varying pH, electrolyte concentration and cation type. Eur. J. Soil
794 Sci. 46, 657–665. doi:DOI: 10.1111/j.1365-2389.1995.tb01362.x
795 Churakov, S. V., Dähn, R., 2012. Zinc adsorption on clays inferred from atomistic simulations
796 and EXAFS spectroscopy. Environ. Sci. Technol. 46, 5713–5719. doi:10.1021/es204423k
797 Ciesielski, H., Sterckeman, T., 1997. Determination of cation exchange capacity and
798 exchangeable cations in soils by means of cobalt hexamine trichloride . agronomie 17, 1–
799 7.
800 Cismasu, A.C., Levard, C., Michel, F.M., Brown, G.E., 2013. Properties of impurity-bearing
801 ferrihydrite II: Insights into the surface structure and composition of pure, Al- and Si-
802 bearing ferrihydrite from Zn(II) sorption experiments and Zn K-edge X-ray absorption
803 spectroscopy. Geochim. Cosmochim. Acta 119, 46–60. doi:10.1016/j.gca.2013.05.040

804 Cornell, R.M., Schwertmann, U., 2003. The Iron Oxides: Structure, Properties, Reactions and
805 Uses, Weinheim: Wiley-VCH. doi:10.1016/j.tca.2005.08.011
806 Covelo, E.F., Vega, F.A., Andrade, M.L., 2007. Heavy metal sorption and desorption capacity
807 of soils containing endogenous contaminants. J. Hazard. Mater. 143, 419–430.
808 doi:10.1016/j.jhazmat.2006.09.047
809 Dähn, R., Baeyens, B., Bradbury, M.H., 2011. Investigation of the different binding edge sites
810 for Zn on montmorillonite using P-EXAFS - The strong/weak site concept in the 2SPNE
811 SC/CE sorption model. Geochim. Cosmochim. Acta 75, 5154–5168.
812 doi:10.1016/j.gca.2011.06.025
813 Davis, J.A., Coston, J.A., Kent, D.B., Fuller, C.C., 1998. Application of the surface
814 complexation concept to complex mineral assemblages. Environ. Sci. Technol. 32, 2820–
815 2828. doi:10.1021/es980312q
816 Dyer, J.A., Trivedi, P., Scrivner, N.C., Sparks, D.L., 2004. Surface complexation modeling of
817 zinc sorption onto ferrihydrite. J. Colloid Interface Sci. 270, 56–65. doi:10.1016/S0021-
818 9797(03)00618-0
819 Elzinga, E.J., Reeder, R.J., 2002. X-ray absorption spectroscopy study of Cu2+and
820 Zn2+adsorption complexes at the calcite surface: Implications for site-specific metal
821 incorporation preferences during calcite crystal growth. Geochim. Cosmochim. Acta 66,
822 3943–3954. doi:10.1016/S0016-7037(02)00971-7
823 Elzinga, E.J., Rouff, A.A., Reeder, R.J., 2006. The long-term fate of Cu2+, Zn2+, and Pb2+
824 adsorption complexes at the calcite surface: An X-ray absorption spectroscopy study.
825 Geochim. Cosmochim. Acta 70, 2715–2725. doi:10.1016/j.gca.2006.02.026
826 Ferreira, J.R., Lawlor, A.J., Bates, J.M., Clarke, K.J., Tipping, E., 1997. Chemistry of riverine
827 and estuarine suspended particles from the Ouse-Trent system, UK. Colloids Surfaces A
828 Physicochem. Eng. Asp. 120, 183–198. doi:10.1016/S0927-7757(96)03721-1

829 Ford, R.G., Sparks, D.L., 2000. The nature of Zn precipitates formed in the presence of
830 pyrophyllite. Environ. Sci. Technol. 34, 2479–2483. doi:10.1021/es991330q
831 Green-Pedersen, H., Pind, N., 2000. Preparation, characterization, and sorption properties for
832 Ni(II) of iron oxyhydroxide-montmorillonite. Colloids Surfaces A Physicochem. Eng.
833 Asp. 168, 133–145. doi:10.1016/S0927-7757(00)00448-9
834 Grosbois, C., Meybeck, M., Lestel, L., Lefèvre, I., Moatar, F., 2012. Severe and contrasted
835 polymetallic contamination patterns (1900-2009) in the Loire River sediments (France).
836 Sci. Total Environ. 435–436, 290–305. doi:10.1016/j.scitotenv.2012.06.056
837 Hofmann, A., Vantelon, D., Montargès-Pelletier, E., Villain, F., Gardoll, O.,
838 Razafitianamaharavo, A., Ghanbaja, J., 2013. Interaction of Fe(III) and Al(III) during
839 hydroxylation by forced hydrolysis: The nature of Al-Fe oxyhydroxy co-precipitates. J.
840 Colloid Interface Sci. 407, 76–88. doi:10.1016/j.jcis.2013.06.020
841 Isaure, M.P., Laboudigue, A., Manceau, A., Sarret, G., Tiffreau, C., Trocellier, P., Lamble, G.,
842 Hazemann, J.L., Chateigner, D., 2002. Quantitative Zn speciation in a contaminated
843 dredged sediment by μ-PIXE, μ-SXRF, EXAFS spectroscopy and principal component
844 analysis. Geochim. Cosmochim. Acta 66, 1549–1567. doi:10.1016/S0016-
845 7037(01)00875-4
846 Jacquat, O., Voegelin, A., Kretzschmar, R., 2009. Local coordination of Zn in hydroxy-
847 interlayered minerals and implications for Zn retention in soils. Geochim. Cosmochim.
848 Acta 73, 348–363. doi:10.1016/j.gca.2008.10.026
849 Jacquat, O., Voegelin, A., Villard, A., Marcus, M.A., Kretzschmar, R., 2008. Formation of Zn-
850 rich phyllosilicate, Zn-layered double hydroxide and hydrozincite in contaminated
851 calcareous soils. Geochim. Cosmochim. Acta 72, 5037–5054.
852 doi:10.1016/j.gca.2008.07.024
853 Juillot, F., Marechal, C., Morin, G., Jouvin, D., Cacaly, S., Telouk, P., Benedetti, M.F.,

854 Ildefonse, P., Sutton, S., Guyot, F., Brown, G.E., 2011. Contrasting isotopic signatures
855 between anthropogenic and geogenic Zn and evidence for post-depositional fractionation
856 processes in smelter-impacted soils from Northern France. Geochim. Cosmochim. Acta
857 75, 2295–2308. doi:10.1016/j.gca.2011.02.004
858 Juillot, F., Morin, G., Ildefonse, P., Calas, G., Brown, G.E., 2006. EXAFS signature of
859 structural Zn at trace levels in natural and synthetic trioctahedral 2:1 phyllosilicates. Am.
860 Mineral. 91, 1432–1441. doi:10.2138/am.2006.1923
861 Kaufhold, S., Färber, G., Dohrmann, R., Ufer, K., Grathoff, G., 2015. Zn-rich smectite from
862 the Silver Coin Mine, Nevada, USA. Clay Miner. 50, 417–430.
863 doi:10.1180/claymin.2015.050.4.01
864 Le Meur, M., 2016. Matières en suspension de la Moselle (Lorraine , France) : caractérisation
865 minérale et organique et réactivité vis-à-vis des contaminants métalliques. Université de
866 Lorraine.
867 Le Meur, M., Mansuy-Huault, L., Lorgeoux, C., Bauer, A., Gley, R., Vantelon, D., Montargès-
868 Pelletier, E., 2017. Spatial and temporal variations of Particulate Organic Matter from
869 Moselle River and tributaries: A multimolecular investigation. Org. Geochem. 110, 45–
870 56. doi:10.1016/j.orggeochem.2017.04.003
871 Le Meur, M., Montargès-Pelletier, E., Bauer, A., Gley, R., Migot, S., Barres, O., Delus, C.,
872 Villiéras, F., 2016. Characterization of suspended particulate matter in the Moselle River
873 (Lorraine, France): evolution along the course of the river and in different hydrologic
874 regimes. J. Soils Sediments 16, 1625–1642. doi:10.1007/s11368-015-1335-8
875 Le Pape, P., Ayrault, S., Quantin, C., 2012. Trace element behavior and partition versus
876 urbanization gradient in an urban river (Orge River, France). J. Hydrol. 472–473, 99–110.
877 doi:10.1016/j.jhydrol.2012.09.042
878 Le Pape, P., Quantin, C., Morin, G., Jouvin, D., Kieffer, I., Proux, O., Ghanbaja, J., Ayrault, S.,

879 2014. Zinc speciation in the suspended particulate matter of an urban river (Orge, France):
880 Influence of seasonality and urbanization gradient. Environ. Sci. Technol. 48, 11901–
881 11909. doi:10.1021/es500680x
882 Lead, J.R., Hamilton-Taylor, J., Davison, W., Harper, M., 1999. Trace metal sorption by natural
883 particles and coarse colloids. Geochim. Cosmochim. Acta 63, 1661–1670.
884 doi:10.1016/S0016-7037(99)00006-X
885 Lee, S., Anderson, P.R., Bunker, G.B., Karanfil, C., 2004. EXAFS study of Zn sorption
886 mechanisms on montmorillonite. Environ. Sci. Technol. 38, 5426–5432.
887 doi:10.1021/es0350076
888 Liljestrand, H.M., Lo, I.M.C., Shimizu, Y., 1992. Sorption of humic materials onto inorganic
889 surfaces for the mitigation of facilitated pollutant transport processes, in: Water Science
890 and Technology. doi:10.1016/j.nuclcard.2007.04.014
891 Luo, Y., Giammar, D.E., Huhmann, B.L., Catalano, J.G., 2011. Speciation of selenium, arsenic,
892 and zinc in Class C fly ash. Energy and Fuels 25, 2980–2987. doi:10.1021/ef2005496
893 Manceau, A., Boisset, M.C., Sarret, G., Hazemann, J.L., Mench, M., Cambier, P., Prost, R.,
894 1996. Direct determination of lead speciation in contaminated soils by EXAFS
895 spectroscopy. Environ. Sci. Technol. 30, 1540–1552. doi:10.1021/es9505154
896 Manickam, S., Barbaroux, L., Ottman, F., 1985. Composition and mineralogy of suspended
897 sediment in the fluvio-estuarine zone of the Loire River, France. Sedimentology 32, 721–
898 741. doi:10.1111/j.1365-3091.1985.tb00484.x
899 Minaberry, Y.S., Gordillo, G.J., 2010. The influence of organic ligands on the adsorption of
900 cadmium by suspended matter in natural waters studied by matrix-assisted laser
901 desorption/ionization time-of-flight mass spectrometry and electrochemical methods.
902 Chemosphere 78, 1356–1361. doi:10.1016/j.chemosphere.2010.01.004
903 Minaberry, Y.S., Gordillo, G.J., 2007. Complexing capacity of natural waters carrying a great

amount of suspended matter. Chemosphere 69, 1465–1473. doi:10.1016/j.chemosphere.2007.04.058

Miyazaki, A., Balint, I., Nakano, Y., 2003. Solid-liquid interfacial reaction of Zn2+ ions on the surface of amorphous aluminosilicates with various Al/Si ratios. Geochim. Cosmochim. Acta 67, 3833–3844. doi:10.1016/S0016-7037(03)00373-9

Montoya, V., Baeyens, B., Glaus, M.A., Kupcik, T., Marques Fernandes, M., Van Laer, L., Bruggeman, C., Maes, N., Schäfer, T., 2018. Sorption of Sr, Co and Zn on illite: Batch experiments and modelling including Co in-diffusion measurements on compacted samples. Geochim. Cosmochim. Acta 223, 1–20. doi:10.1016/j.gca.2017.11.027

Nachtegaal, M., Sparks, D.L., 2004. Effect of iron oxide coatings on zinc sorption mechanisms at the clay-mineral/water interface. J. Colloid Interface Sci. 276, 13–23. doi:10.1016/j.jcis.2004.03.031

Newville, M., 2001. IFEFFIT: Interactive XAFS analysis and FEFF fitting. J. Synchrotron Radiat. 8, 322–324. doi:10.1107/S0909049500016964

Nriagu, J.O., Pacyna, J.M., 1988. Quantitative assessment of worldwide contamination of air, water and soils by trace metals. Nature 333, 134–139. doi:10.1038/333134a0

Orsini, L., Remy, J.C., 1976. Utilisation du chlorure de cobaltihexammine pour la détermination simultanée de la capacité d'échange et des bases échangeables des sols. Bull. l'AFES Sci. du Sol 4, 269–275.

Parfitt, R.L., Giltrap, D.J., Whitton, J.S., 1995. Contribution of organic matter and clay minerals to the cation exchange capacity of soils. Commun. Soil Sci. Plant Anal. 26, 1343–1355. doi:10.1080/00103629509369376

Prélot, B., 2001. Mesure et modélisation de l'hétérogénéité énergétique à l'interface oxyde/électrolyte/métaux.

Prélot, B., Charmas, R., Zarzycki, P., Thomas, F., Villiéras, F., Piasecki, W., Rudziński, W.,

2002. Application of the theoretical 1-pK approach to analyzing proton adsorption isotherm derivatives on heterogeneous oxide surfaces. J. Phys. Chem. B 106, 13280–13286. doi:10.1021/jp0200573

Priadi, C., Le Pape, P., Morin, G., Ayrault, S., Maillot, F., Juillot, F., Hochreutener, R., Llorens, I., Testemale, D., Proux, O., Brown, G.E., 2012. X-ray absorption fine structure evidence for amorphous zinc sulfide as a major zinc species in suspended matter from the Seine river downstream of Paris, Ile-De-France, France. Environ. Sci. Technol. 46, 3712–3720. doi:10.1021/es2041652

Ravel, B., Newville, M., 2005. ATHENA, ARTEMIS, HEPHAESTUS: Data analysis for X-ray absorption spectroscopy using IFEFFIT, in: Journal of Synchrotron Radiation. pp. 537–541. doi:10.1107/S0909049505012719

Resongles, E., Casiot, C., Freydier, R., Le Gall, M., Elbaz-Poulichet, F., 2015. Variation of dissolved and particulate metal(loid) (As, Cd, Pb, Sb, Tl, Zn) concentrations under varying discharge during a Mediterranean flood in a former mining watershed, the Gardon River (France). J. Geochemical Explor. 158, 132–142. doi:10.1016/j.gexplo.2015.07.010

Roussel, H., Briois, V., Elkaim, E., de Roy, A., Besse, J.-P., Jolivet, J.-P., 2001. Study of the Formation of the Layered Double Hydroxide [Zn−Cr−Cl]. Chem. Mater. 13, 329–337. doi:10.1021/cm001066w

Scheinost, A.C., Kretzschmar, R., Pfister, S., Roberts, D.R., 2002. Combining selective sequential extractions, X-ray absorption spectroscopy, and principal component analysis for quantitative zinc speciation in soil. Environ. Sci. Technol. 36, 5021–5028. doi:10.1021/es025669f

Schlegel, M.L., Manceau, A., 2006. Evidence for the nucleation and epitaxial growth of Zn phyllosilicate on montmorillonite. Geochim. Cosmochim. Acta 70, 901–917. doi:10.1016/j.gca.2005.10.021

954 Schlegel, M.L., Manceau, A., Charlet, L., Chateigner, D., Hazemann, J.L., 2001. Sorption of
955 metal ions on clay minerals. III. Nucleation and epitaxial growth of Zn phyllosilicate on
956 the edges of hectorite. Geochim. Cosmochim. Acta 65, 4155–4170. doi:10.1016/S0016-
957 7037(01)00700-1
958 Sipos, P., Kis, V.K., Balázs, R., Tóth, A., Kovács, I., Németh, T., 2018. Contribution of
959 individual pure or mixed-phase mineral particles to metal sorption in soils. Geoderma 324,
960 1–8. doi:10.1016/j.geoderma.2018.03.008
961 Sipos, P., Németh, T., Kis, V.K., Mohai, I., 2008. Sorption of copper, zinc and lead on soil
962 mineral phases. Chemosphere 73, 461–469. doi:10.1016/j.chemosphere.2008.06.046
963 Slomberg, D.L., Ollivier, P., Radakovitch, O., Baran, N., Sani-Kast, N., Miche, H., Borschneck,
964 D., Grauby, O., Bruchet, A., Scheringer, M., Labille, J., 2016. Characterisation of
965 suspended particulate matter in the Rhone River: insights into analogue selection. Environ.
966 Chem. doi:10.1071/EN15065
967 Sondi, I., Bišćan, J., Pravdić, V., 1996. Electrokinetics of pure clay minerals revisited. J. Colloid
968 Interface Sci. 178, 514–522. doi:10.1006/jcis.1996.0146
969 Stumm, W., 1993. Aquatic colloids as chemical reactants: surface structure and reactivity.
970 Colloids Surfaces A Physicochem. Eng. Asp. 73, 1–18. doi:10.1016/0927-
971 7757(93)80003-W
972 Superville, P.J., Louis, Y., Billon, G., Prygiel, J., Omanović, D., Pižeta, I., 2011. An adaptable
973 automatic trace metal monitoring system for on line measuring in natural waters. Talanta
974 87, 85–92. doi:10.1016/j.talanta.2011.09.045
975 Tertre, E., Beaucaire, C., Coreau, N., Juery, A., 2009. Modelling Zn(II) sorption onto clayey
976 sediments using a multi-site ion-exchange model. Appl. Geochemistry 24, 1852–1861.
977 doi:10.1016/j.apgeochem.2009.06.006
978 Thomas, F., Michot, L.J., Vantelon, D., Montargès, E., Prélot, B., Cruchaudet, M., Delon, J.F.,

1999. Layer charge and electrophoretic mobility of smectites, in: Colloids and Surfaces A: Physicochemical and Engineering Aspects. pp. 351–358. doi:10.1016/S0927-7757(99)00291-5

Toner, B., Manceau, A., Webb, S.M., Sposito, G., 2006. Zinc sorption to biogenic hexagonal-birnessite particles within a hydrated bacterial biofilm. Geochim. Cosmochim. Acta 70, 27–43. doi:10.1016/j.gca.2005.08.029

Trivedi, P., Axe, L., Dyer, J., 2001a. Adsorption of metal ions onto goethite: Single-adsorbate and competitive systems. Colloids Surfaces A Physicochem. Eng. Asp. 191, 107–121. doi:10.1016/S0927-7757(01)00768-3

Trivedi, P., Axe, L., Tyson, T. a., 2001b. An Analysis of Zinc Sorption to Amorphous versus Crystalline Iron Oxides Using XAS. J. Colloid Interface Sci. 244, 230–238. doi:10.1006/jcis.2001.7971

Trivedi, P., Dyer, J.A., Sparks, D.L., Pandya, K., 2004. Mechanistic and thermodynamic interpretations of zinc sorption onto ferrihydrite. J. Colloid Interface Sci. doi:10.1016/S0021-9797(03)00586-1

Viers, J., Dupré, B., Gaillardet, J., 2009. Chemical composition of suspended sediments in World Rivers: New insights from a new database. Sci. Total Environ. 407, 853–868. doi:10.1016/j.scitotenv.2008.09.053

Voegelin, A., Scheinost, A.C., Bühlmann, K., Barmettler, K., Kretzschmar, R., 2002. Slow formation and dissolution of Zn precipitates in soil: A combined column-transport and XAFS study. Environ. Sci. Technol. 36, 3749–3754. doi:10.1021/es010316m

Wang, F., Chen, J., Forsling, W., 1997. Modeling sorption of trace metals on natural sediments by surface complexation model. Environ. Sci. Technol. 31, 448–453. doi:10.1021/es960270a

Waychunas, G.A., Fuller, C.C., Davis, J.A., 2002. Surface complexation and precipitate

1004 geometry for aqueous Zn(II) sorption on ferrihydrite I: X-ray absorption extended fine
1005 structure spectroscopy analysis. Geochim. Cosmochim. Acta 66, 1119–1137.
1006 doi:10.1016/S0016-7037(01)00853-5
1007 Waychunas, G.A., Fuller, C.C., Davis, J.A., Rehr, J.J., 2003. Surface complexation and
1008 precipitate geometry for aqueous Zn(II) sorption on ferrihydrite: II. XANES analysis and
1009 simulation. Geochim. Cosmochim. Acta 67, 1031–1043. doi:10.1016/S0016-
1010 7037(02)01280-2
1011 Yin, N.H., Sivry, Y., Benedetti, M.F., Lens, P.N.L., van Hullebusch, E.D., 2015. Application
1012 of Zn isotopes in environmental impact assessment of Zn-Pb metallurgical industries: A
1013 mini review. Appl. Geochemistry 64, 128–135. doi:10.1016/j.apgeochem.2015.09.016
1014 Young, L.B., Harvey, H.H., 1992. The relative importance of manganese and iron oxides and
1015 organic matter in the sorption of trace metals by surficial lake sediments. Geochim.
1016 Cosmochim. Acta 56, 1175–1186. doi:10.1016/0016-7037(92)90055-N
1017 Zhuang, J., Yu, G.R., 2002. Effects of surface coatings on electrochemical properties and
1018 contaminant sorption of clay minerals. Chemosphere 49, 619–628. doi:10.1016/S0045-
1019 6535(02)00332-6
1020 Zimmermann-Timm, H., 2002. Characteristics, Dynamics and Importance of Aggregates in
1021 Rivers - An Invited Review. Int. Rev. Hydrobiol. 87, 197–240. doi:10.1002/1522-
1022 2632(200205)87:2/3<197::AID-IROH197>3.0.CO;2-7
1023
1024

TABLE CAPTIONS

*Table 1. CEC, textural properties for the different SPM and pure minerals, organic matter content and sampling details. CEC (mEq per 100 g) was measured from the adsorption of cobalt-hexamine. Sample names refer to the stations (PSV, FRO, MIL, PAM, ARG, FLO and THI) on the Moselle River and its tributaries. The stations are classified from upstream to downstream, PSV being the most upstream station within the Moselle watershed. See Le Meur et al. 2016 for details about the stations. Textural properties of SPM and model minerals, obtained by nitrogen adsorption measurements. N_2 surface area (SSA-BET, $m^2 g^{-1}$, BET theory), energetic constant C; * from Prelot 2001. Organic matter content was estimated from thermogravimetric curves (see Le Meur et al. 2017). The last column precises the sampled river and the mean dialy water flow at the day of SPM sampling ($m^3 s^{-1}$). NM: not measured. NA: not applicable .*

Table 2 - XANES fitting parameters, linear combinations of reference spectra. FRO-Jul13 and FRO-Dec12 SPM samples before and after Zn adsorption. The suffix « Zni » refers to the different points of the adsorption curves on figure 2, and the 3k suffix means that the batch experiments were conducted with higher ionic strength in solution, electrical conductivity was set to 3000 µS cm-1 by addition of $NaNO_3$ solution (1.2 M). ***N****: number of reference spectra used for fitting,* ***SPM****: spectrum of the pristine SPM sample ;* ***Zn_{low}-illite****: Zn adsorbed onto illite, low loading;* ***Zn_{high}-illite****: Zn adsorbed onto illite, High loading;* ***Smec****: zinciferous smectite;* ***Zn_{low}-calcite****: Zn adsorbed onto calcite, low loading;* ***Zn high calcite****: Zn adsorbed onto calcite, high loading;* ***Zncit****: Zn in aqueous solution, complexed with citrate;* ***Zn_{high}-Goet****: Zn adsorbed onto goethite, high loading;* ***Zn_{high}-FeH:*** *Zn adsorbed onto ferrihydrite, high loading;* ***ZnHDL****: Layered double hydoxide;* ***R_X factor****, multiplied by 10^4,* ***χ^2*** *multiplied by 10^2,* ***Red χ^2*** *multiplied by 10^4 ;* ***[Zn]*** *: amount of adsorbed Zn, mmol kg^{-1}.*

Table 3. Zn adsorbed onto SPM, EXAFS fitting parameters, linear combinations of reference spectra. ***N*** *: number of reference spectra used for fitting,* ***SPM****: spectrum of the pristine SPM sample ;* ***Zn_{low}-illite****: Zn adsorbed onto illite, low loading;* ***Zn_{high}-illite****: Zn adsorbed onto illite, High loading;* ***Zn_{low}-calcite****: Zn adsorbed onto calcite, low loading;* ***Zn_{high}-calcite****: Zn adsorbed onto calcite, high loading;* ***Zn_{high}-FeH :*** *Zn adsorbed onto ferrihydrite, high loading;* ***ZnHDL****: Layered double hydroxide;* ***ZnO****: zincite ;* ***R_X factor****, multiplied by 10^2,* ***χ^2****;* ***Red χ^2****;* ***[Zn]****: Zn content or amount of adsorbed Zn, mmol kg^{-1}.*

Table 4. FRO-JUL 13 - EXAFS fitting parameters, shell by shell fitting using theoretical backscattering curves for the SPM sample FRO-Jul13 and derivatives obtained after Zn sorption. Summary of the local structural parameters derived from EXAFS data analysis (shell by shell fitting). The Zn EXAFS data were Fourier transformed over the k range Δk and fitted over the ΔR range with single scattering paths involving O, Zn or Al atoms. The amplitude reduction factor S_0^2 was fixed to 0.7 but the energy shift was released for fitting. The number of atoms of the first coordination shell was fixed to 6, excepted for the first sample FRO-Jul13. The number of atoms, the distance R and disorder σ^2 were released for all the coordination shells. Parameters with strong correlation factors were not released simultaneously.

Table 5. FRO-DEC 12 - EXAFS fitting parameters, shell by shell fitting using theoretical backscattering curves for the SPM sample FRO-Jul13 and derivatives obtained after Zn sorption. Summary of the local structural parameters derived from EXAFS data analysis (shell by shell fitting). The Zn EXAFS data were Fourier transformed over the k range Δk and fitted over the ΔR range with single scattering paths involving O, Zn or Al atoms. The amplitude reduction factor S_0^2 was fixed to 0.7 but the energy shift was released for fitting. The number of atoms of the first coordination shell was fixed to 6, excepted for the first sample FRO-Jul13. The number of atoms, the distance R and disorder σ^2 were released for all the coordination shells. Parameters with strong correlation factors were not released simultaneously.

FIGURE CAPTIONS

Figure 1. Electrophoretic mobility measured for illite, ferrihydrite (FeH) and two Moselle River SPM samples

Figure 2. Batch experiments of Zn adsorption onto model minerals (A) and onto river SPM samples (B and C). The third graph compares Zn adsorption on SPM using two different ionic strengths, respectively set at 300 and 3000 µS cm^{-1}.

Figure 3. XANES spectra at Zn-K edge for model compounds and for FRO-Jul13 and FRO-Dec12 before and after Zn adsorption.

Left graph, model compounds

(a) Zn smectite, sauconite, provided by Stephan Kaufhold (Kaufhold et al., 2015);

(b) Illite du Puy, purified and size fractionated, Zn content 3.4 mmol kg^{-1};

(c) Zn_{low}-illite, Zn adsorbed onto illite, low Zn loading 5.8 mmol kg^{-1};

(d) Zn_{low}-illite-FeH, Zn adsorbed onto illite-FeH, low Zn loading 2.3 mmol kg^{-1};

(e) Zn_{high}-illite, Zn adsorbed onto illite, high Zn loading 89 mmol kg^{-1};

(f) Zn_{high}-illite-FeH, Zn adsorbed onto illite-FeH, high Zn loading 75 mmol kg^{-1};

(g) Znhigh-Goethite, Zn adsorbed onto Goethite, Zn loading 58 mmol kg^{-1};

(h) Zn_{high}-FeH, Zn adsorbed onto ferrihydrite, high Zn loading 57 mmol kg^{-1}.

(i) Zn_{low}-calcite, Zn adsorbed onto Calcite, low Zn loading 2 mmol kg^{-1};

(j) Zn_{high}-calcite, Zn precipitated onto calcite, Zn:Ca ratio 0.16:1.

(k) Zn double layer hydroxide provided by Valerie Briois (Roussel et al., 2001; Carvalho et al., 2013)

(l) Zn citrate in solution.

Middle graph

(a) FRO-Jul13, Zn content 4.6 mmol kg^{-1}; (b) Zn1, adsorbed Zn 4.1 mmol kg^{-1}; (c) Zn2, adsorbed Zn 20.5 mmol kg^{-1}; (d) Zn3, adsorbed Zn 28.2 mmol kg^{-1}; (e) Zn7, adsorbed Zn 159 mmol kg^{-1}; (f) Zn10, adsorbed Zn 257.5 mmol kg^{-1}; (g) Zn5-3k, adsorbed Zn 74.3 mmol kg^{-1}; (h) Zn7-3k , adsorbed Zn 119.2 mmol kg^{-1}; (i) Zn10-3k , adsorbed Zn 205 mmol kg^{-1}. –

Right graph

(a) FRO-Dec12 Zn content 4 mmol kg^{-1}; (b) Zn1, adsorbed Zn 4.2 mmol kg^{-1}; (c) Zn2, adsorbed Zn 16.2 mmol kg^{-1}; (d) Zn7, adsorbed Zn 138 mmol kg^{-1}; (e) Zn10, adsorbed Zn 214 mmol kg^{-1}; (f) Zn5-3k, adsorbed Zn 71.7 mmol kg^{-1}; (g) Zn7-3k, adsorbed Zn 117.6 mmol kg^{-1}. The suffix "-3k" refers to Zn adsorption experiments performed with higher ionic strength, i.e., electric conductivity was set to 3000 µS cm^{-1} instead of 300 µS cm^{-1}.

Figure 4: EXAFS Oscillations k^3 $\chi(k)$ for reference samples. (a) zincite; (b) Zn smectite-sauconite; (c) illite, Zn content 220 mg kg^{-1}; (d) Zn_{low}-illite, Zn adsorbed onto illite, low Zn loading 3 mmol kg^{-1}; (e) Zn_{high}-illite, Zn adsorbed onto illite, high Zn loading 89 mmol kg^{-1}; (f) Zn_{low}-calcite, Zn adsorbed onto Calcite, low Zn loading 2 mmol kg^{-1}; (g) Zn_{high}-calcite, Zn precipitated onto calcite, Zn:Ca ratio 0.16:1; (h) Zn_{high}-FeH, Zn adsorbed onto ferrihydrite, high Zn loading 57 mmol kg^{-1}; (i) Zn citrate in aqueous solution; (j) Zn double layer hydroxide provided by Valerie Briois (Roussel et al., 2001; Carvalho et al., 2013); (k) amorphous ZnS.

Figure 5. EXAFS and corresponding Fourier transform (magnitude and imaginary parts) for FRO-Jul13 before and after Zn adsorption. Experimental curves and Linear Combination fitting curves – (a) FRO-Jul13; (b) FRO-Jul13 Zn1; (c) FRO-Jul13 Zn2; (d) FRO-Jul13 Zn3; (e) FRO-Jul13 Zn7; (f) FRO-Jul13 Zn10.

Figure 6. EXAFS and corresponding Fourier transform (magnitude and imaginary parts) FRO-Dec12 before and after Zn adsorption. Experimental and Linear Combination Fitting curves – (a) FRO-Dec12; (b) FRO-Dec12 Zn2; (c) FRO-Dec12 Zn7; (d) FRO-Dec12 Zn10.

*Figure 7: Shell by shell fitting, Zn adsorbed onto SPM FRO-Jul13. Experimental (black full line) and theoretical (red dashed line) EXAFS oscillations k^3*chi(k) and Fourier Transform (amplitude and imaginary parts) for FROjul13 before and after Zn adsorption with increasing Zn loading: (a) FRO-Jul13, (b) FRO-Jul13 Zn1, (c) FRO-Jul13 Zn2, (d) FRO-Jul13 Zn3, (e) FRO-Jul13 Zn7, (f) FRO-Jul13 Zn10.*

*Figure 8: Shell by shell fitting, Zn adsorbed onto SPM FRO-Dec12. Experimental (black full line) and Theoretical (red dashed line) EXAFS oscillations k^3*chi(k) and Fourier Transform (amplitude and imaginary parts) for FRO-Dec12 before and after Zn adsorption with increasing Zn loading: (a) FRO-Dec12, (b) FRO-Dec12 Zn2, (c) FRO-Dec12 Zn7, (d) FRO-Dec12 Zn10.*

figure 1

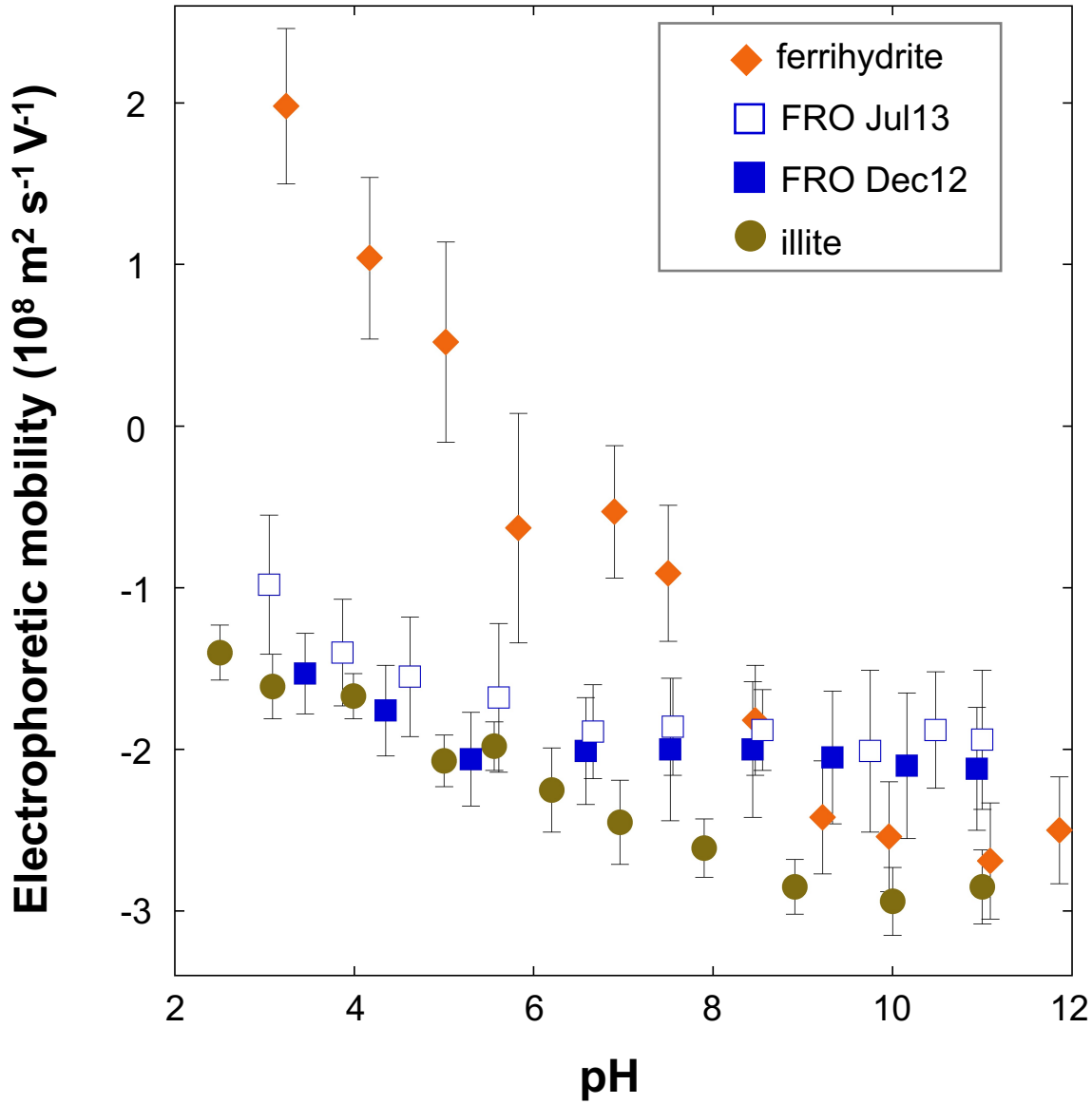
ferrihydrite
FRO Jul13
FRO Dec12
illite
Electrophoretic mobility (10⁸ m² s⁻¹ V⁻¹)
pH
2
1
0
-1
-2
-3
2
4
6
8
10
12

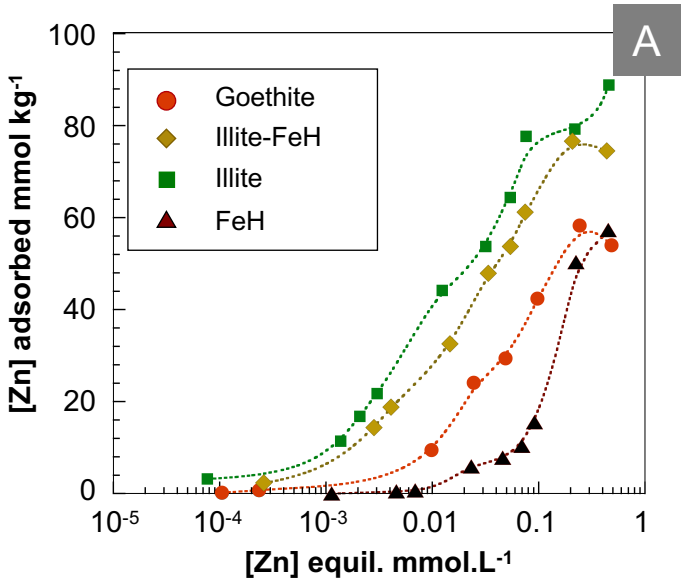
A
Goethite
Illite-FeH
Illite
FeH
[Zn] adsorbed mmol kg-1
[Zn] equil. mmol.L-1
0
20
40
60
80
100
10-5
10-4
10-3
0.01
0.1
1

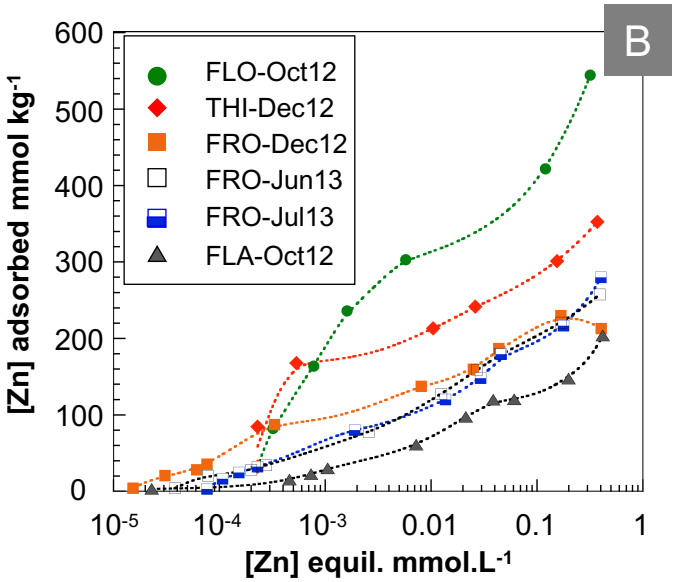
B
FLO-Oct12
THI-Dec12
FRO-Dec12
FRO-Jun13
FRO-Jul13
FLA-Oct12
[Zn] adsorbed mmol kg-1
[Zn] equil. mmol.L-1
0
100
200
300
400
500
600
10-5
10-4
10-3
0.01
0.1
1

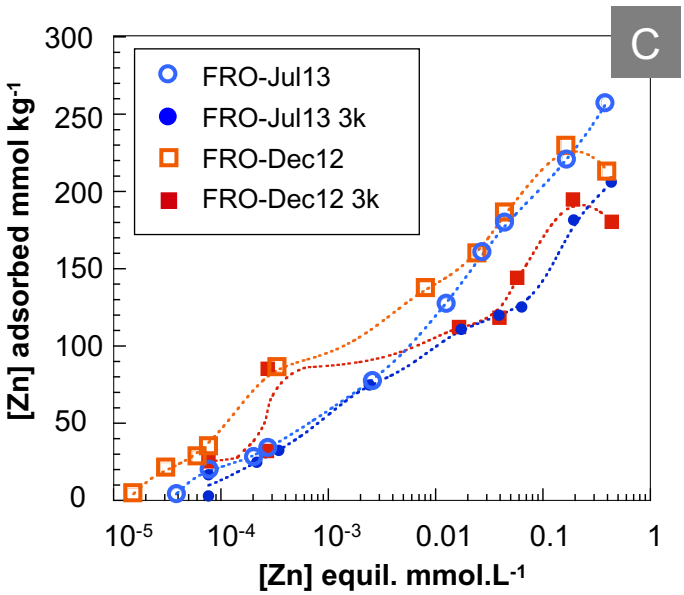
C
FRO-Jul13
FRO-Jul13 3k
FRO-Dec12
FRO-Dec12 3k
[Zn] adsorbed mmol kg-1
[Zn] equil. mmol.L-1
0
50
100
150
200
250
300
10-5
10-4
10-3
0.01
0.1
1

figure 2

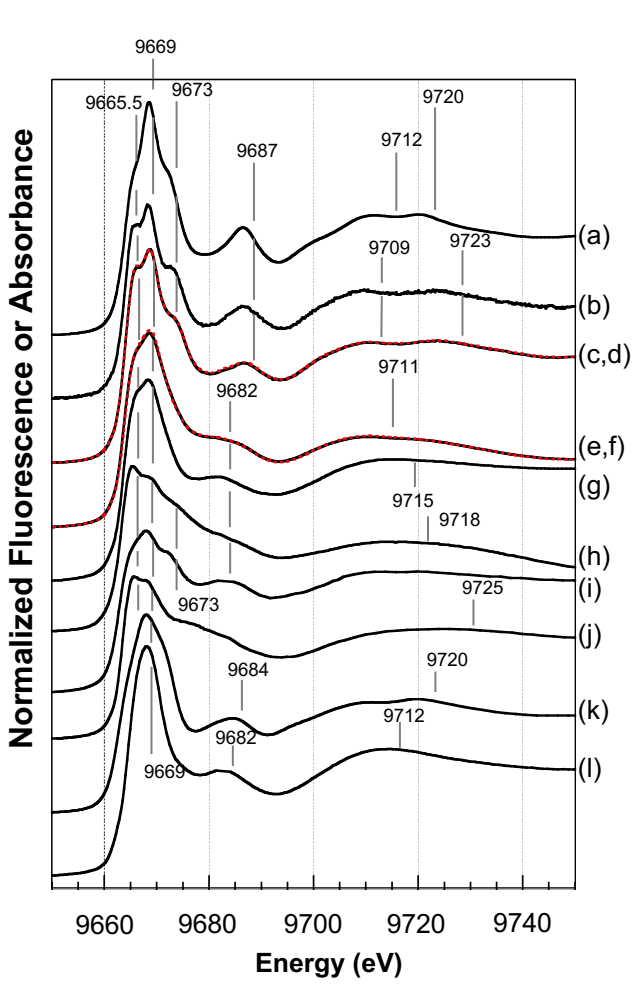
9669
9665.5
9673
9687
9712
9720
9709
9723
(a)
(b)
(c,d)
9711
9682
(e,f)
(g)
9715
9718
(h)
(i)
9673
9725
(j)
9684
9720
(k)
9712
9682
9669
(l)
Normalized Fluorescence or Absorbance
9660
9680
9700
9720
9740
Energy (eV)

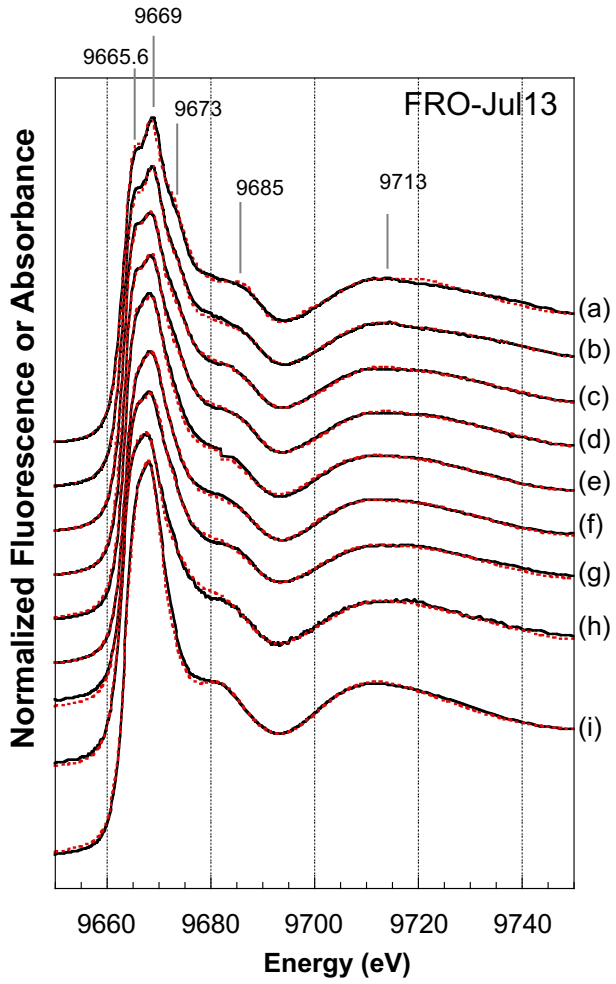
9669
9665.6
FRO-Jul13
9673
9685
9713
(a)
(b)
(c)
(d)
(e)
(f)
(g)
(h)
(i)
Normalized Fluorescence or Absorbance
9660
9680
9700
9720
9740
Energy (eV)

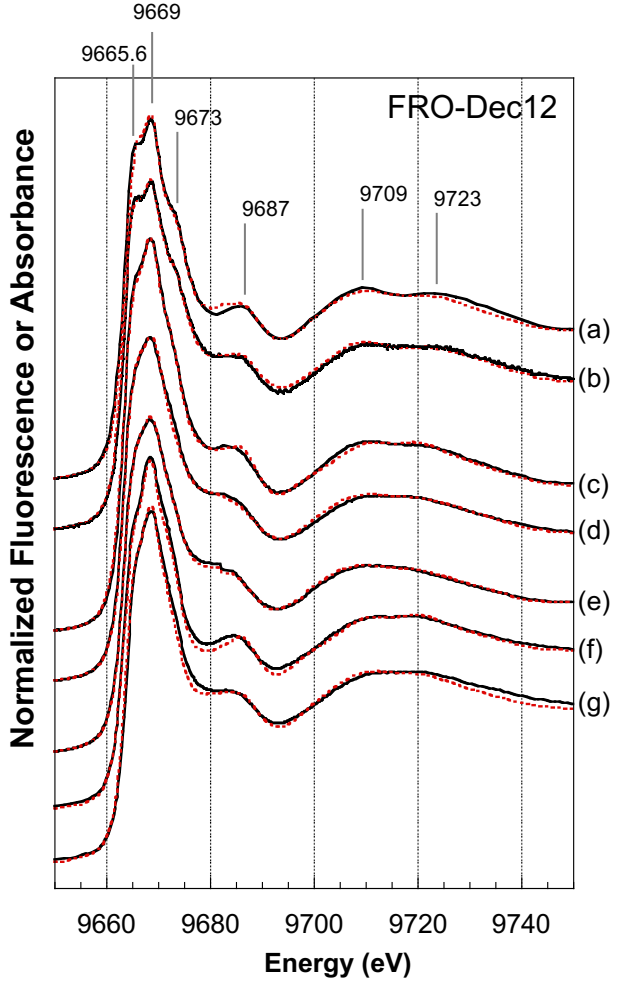
9669
9665.6
FRO-Dec12
9673
9687
9709
9723
(a)
(b)
(c)
(d)
(e)
(f)
(g)
Normalized Fluorescence or Absorbance
9660
9680
9700
9720
9740
Energy (eV)

figure 3

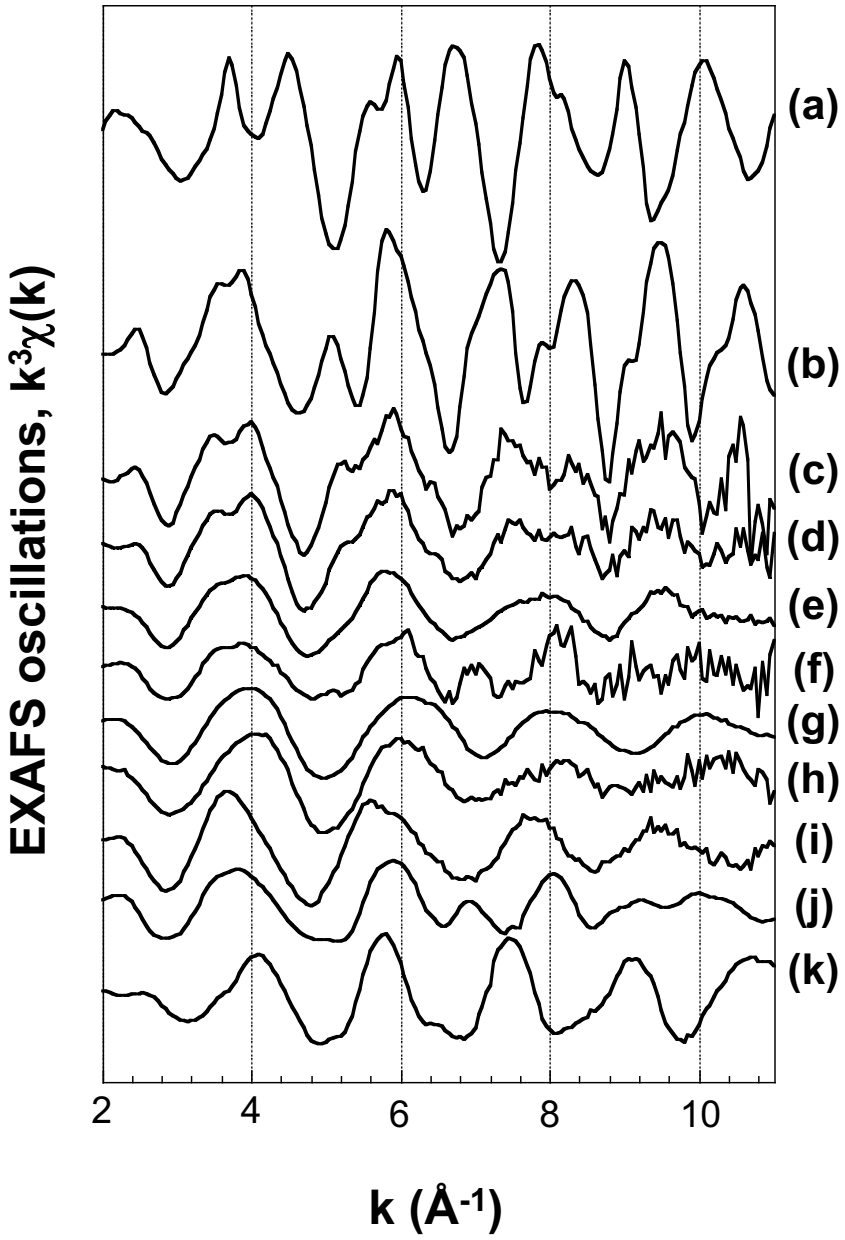

figure 4

figure 5

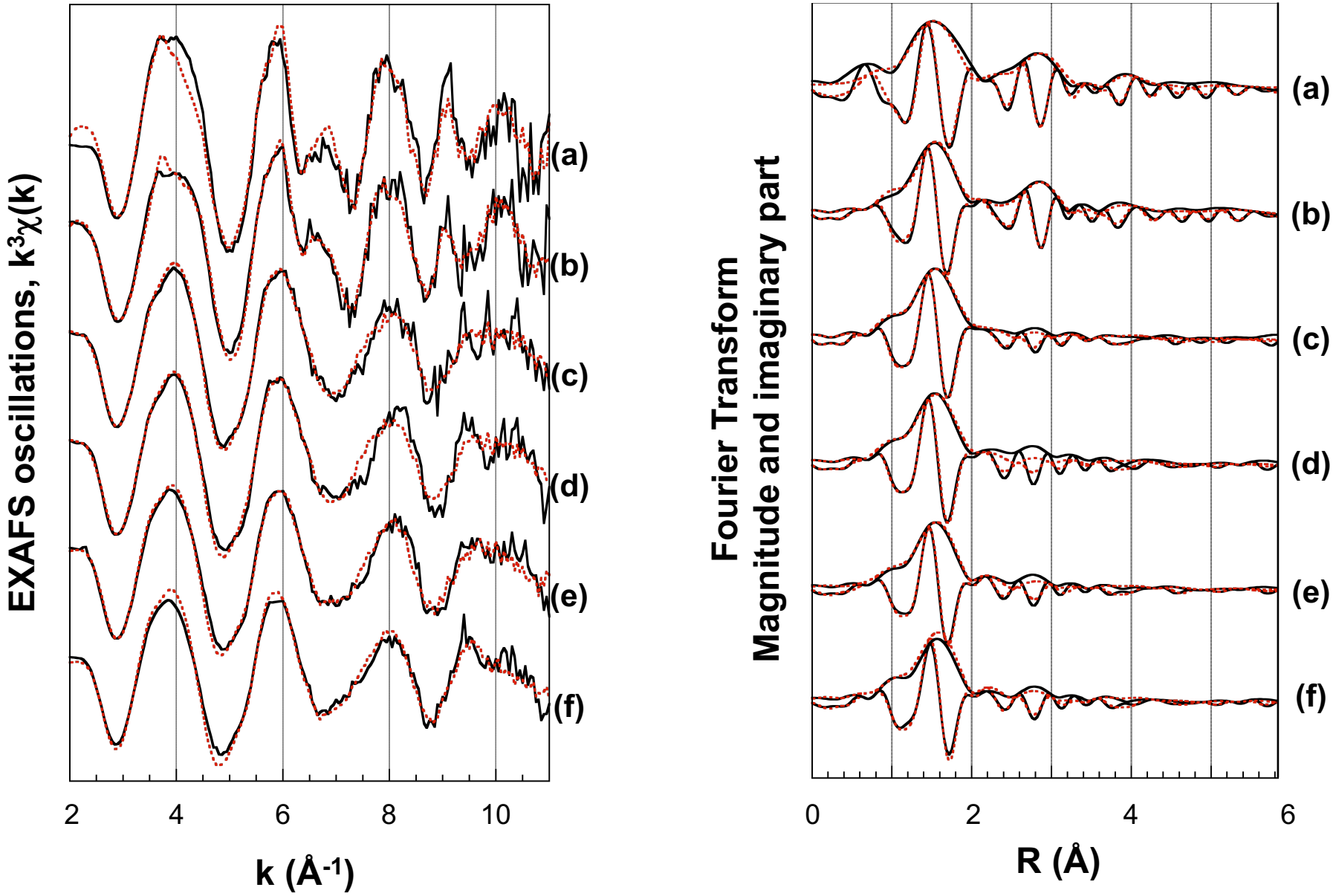
EXAFS oscillations, k³χ(k)
(a)
(b)
(c)
(d)
(e)
(f)
2
4
6
8
10
k (Å-1)
Fourier Transform
Magnitude and imaginary part
(a)
(b)
(c)
(d)
(e)
(f)
0
2
4
6
R (Å)

figure 6

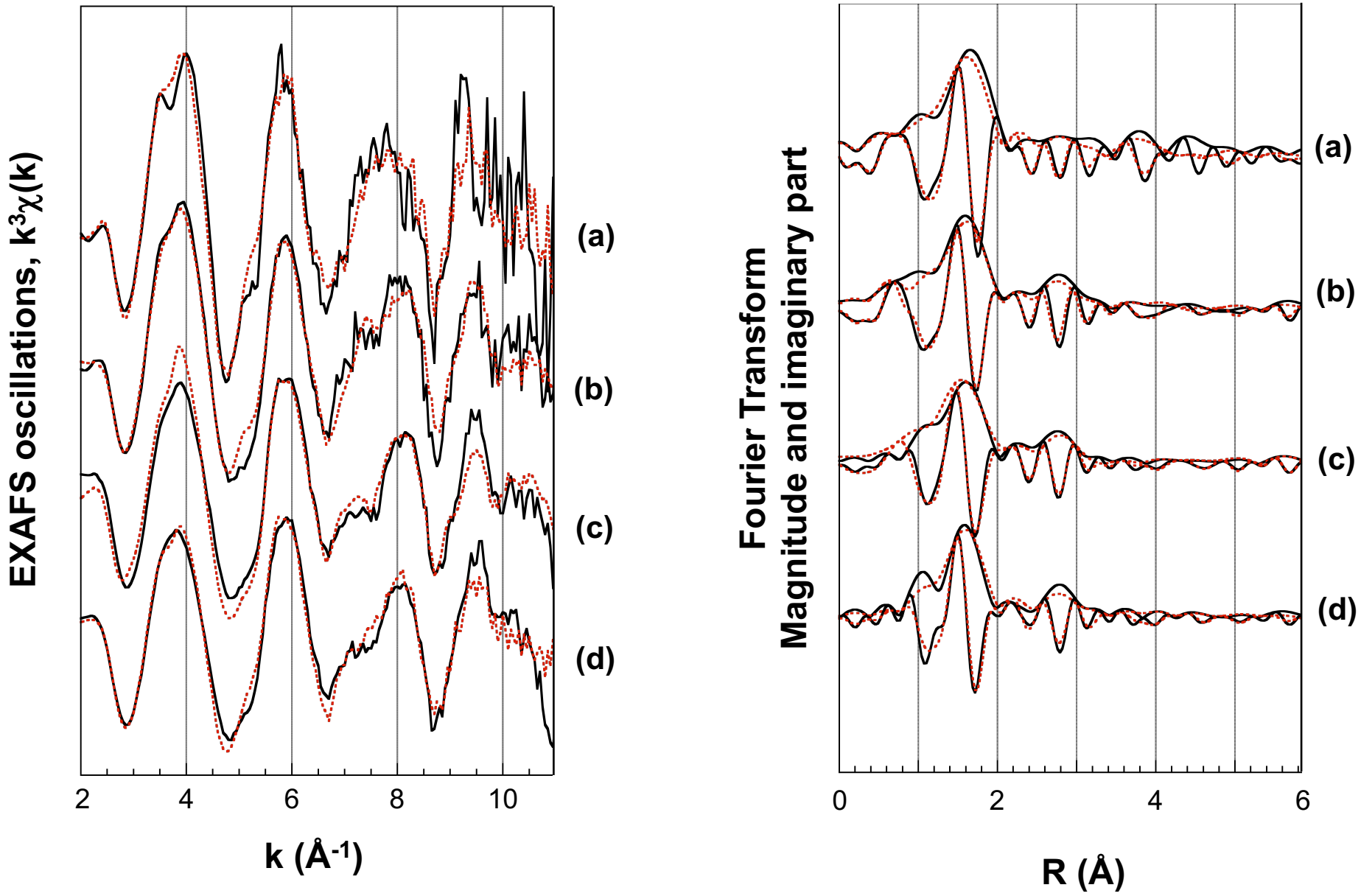
EXAFS oscillations, k³χ(k)
2
4
6
8
10
k (Å⁻¹)
(a)
(b)
(c)
(d)
Fourier Transform
Magnitude and imaginary part
0
2
4
6
R (Å)
(a)
(b)
(c)
(d)

figure 7

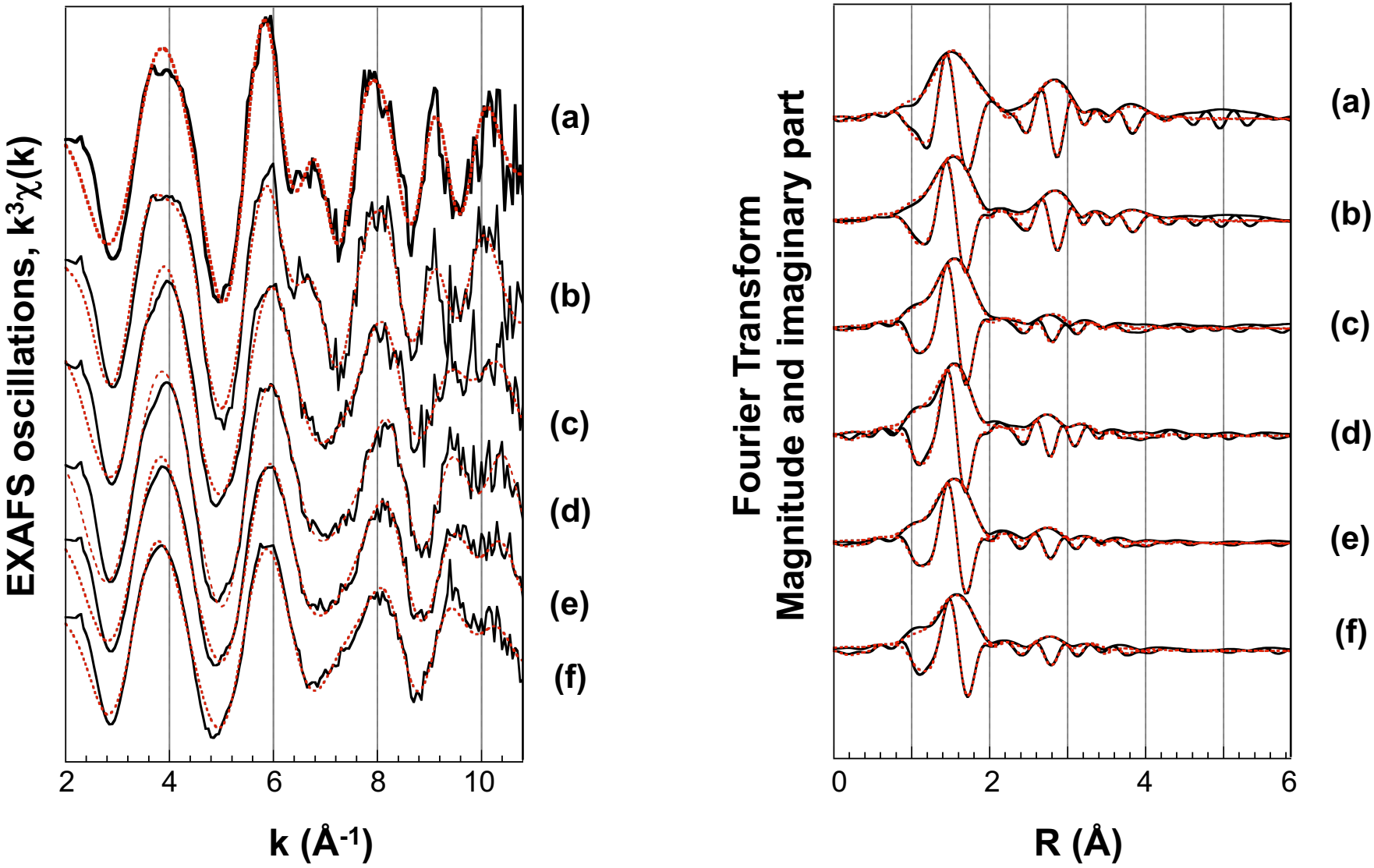
EXAFS oscillations, k³χ(k)
(a)
(b)
(c)
(d)
(e)
(f)
2
4
6
8
10
k (Å-1)
Fourier Transform
Magnitude and imaginary part
(a)
(b)
(c)
(d)
(e)
(f)
0
2
4
6
R (Å)

Table 1. CEC, textural properties for the different SPM samples and pure minerals, organic matter content and sampling details. CEC (mEq per 100 g) was measured from the adsorption of cobalt-hexamine. Sample names refer to the stations (PSV, FRO, MIL, PAM, ARG, FLO and THI) on the Moselle River and its tributaries. The stations are classified from upstream to downstream, PSV being the most upstream station within the Moselle watershed. See Le Meur et al. 2016 for details about the stations. Textural properties of SPM and model minerals, obtained by nitrogen adsorption measurements. N_2 surface area (SSA-BET, $m^2\ g^{-1}$, BET theory), energetic constant C; * from Prelot 2001. Organic matter content was estimated from thermogravimetric curves (see Le Meur et al. 2017). The last column precises the sampled river and the mean daily water flow at the day of SPM sampling ($m^3\ s^{-1}$). NM: not measured. NA: not applicable. FRO samples are classified as a function of organic matter content.

sample	CEC mean value (meq per 100 g)	SSA-BET ($m^2\ g^{-1}$)	C, energetic constant	microporous surface ($m^2\ g^{-1}$)	Organic matter content %	River and Qmd water flow
FeH	NM	218	172	47.6	0	NA
Illite T3	20.3	155	177	28	0	NA
illite-FeH	NM	124	151	28.5	0	NA
Goethite*	NM	18	NA	0	0	NA
FLA-Nov12	NM	15.5	129	1.15	10.8	Moselle 70
PSV-Dec12	42.8	35.5	104	1.1	5.1	Madon 27
PSV-Nov12	28.9	37	114	1.1	5.9	Madon 7
FRO-Dec12	39	31.9	85	Non micr.	5.0	Moselle 397
FRO-Feb14	38.3	32	95	1.2	5.6	Moselle 124
FRO-Nov12	35.2	32.3	66	Non micr.	7.0	Moselle 82
FRO-Jun13	43.6	24.4	70	Non micr.	7.6	Moselle 35
FRO-Jul13	46.7	17.2	85	0.8	8	Moselle 15
MIL-Nov12	31.7	NM	NM	NM	NM	Moselle 233
PAM-Feb13	33.9	32.9	118	1.3	5.2	Moselle 156
PAM-Nov12	42.0	24.4	70	Non micr.	7.5	Moselle 81
ARG-Nov12	40.4	22.9	94	1.0	NM	Moselle 185
FLO-Oct12	37.4	7.4	49	Non micr.	17.4	Fensch 0.6
THI-Dec12	41.6	28	88	Non micr.	6.0	Moselle 200

TABLE 2 - XANES fitting parameters, linear combinations of reference spectra.

XANES spectra fitting, FRO-Jul13 and FRO-Dec12 SPM samples before and after Zn adsorption. The suffix « Zni » refers to the different points of the adsorption curves on figure 2, and the 3k suffix means that the batch experiments were conducted with higher ionic strength in solution, electrical conductivity was set to 3000 µS.cm-1 by addition of $NaNO_3$ solution (1.2 M).
N: number of reference spectra used for fitting, **SPM**: spectrum of the pristine SPM sample ; **Zn_{low}-illite**: Zn sorbed onto illite, low loading; **Zn_{high}-illite**: Zn sorbed onto illite, High loading; **Smec**: zinciferous smectite; **Zn_{low}-calcite**: Zn sorbed onto calcite, low loading; **Zn high calcite**: Zn sorbed onto calcite, high loading; **Zn_{low}-apatite**: Zn sorbed onto apatite, low loading; **Zn_{high}-apatite**: Zn sorbed onto apatite, high loading; **Zncit** : Zn in aqueous solution, complexed with citrate; **Zn_{high}-Goet**: Zn sorbed onto goethite, high loading; **Zn_{high}-FeH :** Zn sorbed onto ferrihydrite, high loading; **ZnHDL**: Layered double hydoxide; **ZnO**: zincite ; **R_X factor**, multiplied by 10^4, **χ^2** multiplied by 10^2, **Red χ^2** multiplied by 10^4 ; **[Zn]** : amount of sorbed Zn, $mmol.kg^{-1}$.

Sample / Reference	N	SPM	Zn low illite	Zn high illite	Smec	Zn high calcite	Zn low calcite	Zn cit	Zn high Goet	Zn high FeH	Zn HDL	R_X ($*10^4$)	χ^2	Red χ^2	[Zn]
a- FRO-Jul13	*3*			*0.09*	*0.27*					*0.64*		*15.3*	*11.5*	*4.3*	4.6
b- *FRO-Jul13* Zn1	2	0.91				0.09						6.7	5.1	1.9	4.1
c- *FRO-Jul13* Zn2	3	0.41						0.14		0.45		7.0	5.4	2.0	20.5
d- *FRO-Jul13* Zn3	3	0.49						0.14		0.37		10	7.7	2.8	28.2
e- *FRO-Jul13* Zn7	2			0.62						0.38		4.7	3.2	1.2	159.1
f- *FRO-Jul13* Zn10	3			0.68				0.06		0.26		3	2.1	0.8	257.5
g- *FRO-Jul13* Zn5-3k	3			0.37					0.25	0.38		21	11.5	3	74.3
h- *FRO-Jul13* Zn7 3k	2							0.34		0.66		17	16	5	119.2
i- *FRO-Jul13* Zn10 3k	2							0.39	0.61			21	26	7	204.9
a-FROdec12	*2*		*0.54*				*0.46*					*29.1*	*19.4*	*12*	4.0
b- FRO-Dec12 Zn1	2	0.73					0.27					18	21	3.6	2.9
c- FRO-Dec12 Zn2	3				0.30					0.52	0.18	8.6	7.3	2.7	16.2
d- FRO-Dec12 Zn7	2			0.69			0.12			0.19		4.4	3.0	1.0	137.8
e- FRO-Dec12 Zn10	2			0.71			0.29					6	3.5	1	214.2
f- FRO-Dec12 Zn5-3k	3				0.38					0.33	0.29	60	34	10	71.7
g- FRO-Dec12 Zn7-3k	3		0.29	0.44							0.27	70	44	13	117.6

Table 3. Zn adsorbed onto SPM samples, EXAFS fitting parameters, linear combinations of reference spectra.

N : number of reference spectra used for fitting, **SPM**: spectrum of the pristine SPM sample ; **Zn_{low}-illite**: Zn sorbed onto illite, low loading; **Zn_{high}-illite**: Zn sorbed onto illite, High loading; **Zn_{low}-calcite**: Zn sorbed onto calcite, low loading; **Zn_{high}-calcite**: Zn sorbed onto calcite, high loading; **Zn_{high}-FeH :** Zn sorbed onto ferrihydrite, high loading; **ZnHDL**: Layered double hydoxide; **ZnO**: zincite ; **R_x factor**, multiplied by 10^2 ; χ^2 , **Red χ^2** ; **[Zn]**: amount of adsorbed Zn, mmol kg^{-1}.

Sample / Reference	N	Zn low Illite	Zn high Illite	Zn high calcite	Zn low calcite	FeH ZnH	Zn HDL	ZnO	R_E ($*10^2$)	χ^2	Red χ^2	[Zn]
a- FRO-Jul13	*3*	*0.5*				*0.25*		*0.25*	*9.5*	*98*	*0.71*	4.6
b- FRO-Jul13 Zn1	3		0.46			0.34		0.2	5.1	42	0.30	4.1
c- FRO-Jul13 Zn2	3		0.45	0.21		0.34			4.7	32	0.23	20.5
d- FRO-Jul13 Zn3	3		0.49	0.26		0.25			5.6	40	0.29	28.2
e- FRO-Jul13 Zn7	3		0.49	0.35	0.16				3	18	0.13	159.1
f- FRO-Jul13 Zn10	3		0.69	0.19			0.12		3.6	19	0.14S	257.5
a- FRO-Dec12	*3*	*0.73*					*0.21*	*0.06*	*12.2*	*153*	*1.10*	4.0
b- FRO-Dec12 Zn2	3		0.37			0.27	0.36		4.7	46	0.33	16.2
c- FRO-Dec12 Zn7	3			0.27		0.20	0.53		7.1	48	0.35	137.8
d- FRO-Dec12 Zn10	3		0.44	0.24			0.32		3.7	27	0.19	214.2

Table 4. FRO-JUL 13 - EXAFS fitting parameters, shell by shell fitting using theoretical backscattering curves for the SPM sample FRO-Jul13 and derivatives obtained after Zn sorption. Summary of the local structural parameters derived from EXAFS data analysis (shell by shell fitting). The Zn EXAFS data were Fourier transformed over the k range Δk and fitted over the ΔR range with single scattering paths involving O, Zn or Al atoms. The amplitude reduction factor S_0^2 was fixed to 0.7 but the energy shift was released for fitting. The number of atoms of the first coordination shell was fixed to 6, excepted for the first sample FRO-Jul13. The number of atoms, the distance R and disorder σ^2 were released for all the coordination shells. Parameters with strong correlation factors were not released simultaneously.

	Fitting range Δk(Å^{-1})	Fitting range ΔR (Å)	shell	Number of atoms	R(Å)	σ^2 (Å^2)	ΔE (eV)	S_0^2	R factor
FRO-Jul13	2.8-10.9	1-4.3	Zn-O	5	1.99±0.01	0.007±0.001	-1.0 ± 0.2	0.70	0.0003
			Zn-S	0.9±0.2	2.32±0.01	0.004±0.002			
			Zn-Zn	3±1	3.18 ±0.02	0.012±0.0012			
			Zn-O	1.32±1	3.77 ±0.02	0.009±0.001			
			Zn-Zn	1±0.5	4.15±0.02	0.011±0.002			
			Zn-O	5±1	4.52±0.02	0.006±0.0015			
FRO-Jul13 Zn1	2.8-10.9	1-4.3	Zn-O	6.0	2.0±0.01	0.0098±0.001	0.5 ± 0.2	0.70	0.0002
			Zn-Zn	3.5	3.19±0.01	0.010±0.002			
			Zn-O	3.4±1	3.78±0.01	0.008±0.002			
			Zn-Zn	0.7±0.6	3.78±0.012	0.011±0.002			
			Zn-O	3.3±1	4.14±0.015	0.011±0.002			
FRO-Jul13 Zn2	2.8-10.9	1-3.5	Zn-O	6	2.0±0.005	0.01±0.001	1.7 ± 0.3	0.70	0.00007
			Zn-Zn	0.9±0.7	3.13±0.006	0.008±0.002			
			Zn-Al	2±1	3.62±0.02	0.013±0.002			
FRO-Jul13 Zn3	2.8-10.9	1-4.1	Zn-O	6	5.9	0.011±0.001	-0.5 ± 0.2	0.70	0.0007
			Zn-Zn	1±0.3	3.10±0.02	0.0048±0.0015			
			Zn-Al	1.4±0.5	3.58±0.02	0.0073±0.001			
FRO-Jul13 Zn7	2.8-10.9	1-3.9	Zn-O	6.0	2.01±0.01	0.009±0.001	-0.12 ± 0.2	0.7	0.0004
			Zn-Zn	1.0±0.3	3.10±0.01	0.0062±0.0005			
			Zn-O	2±0.5	3.66±0.01	0.008±0.001			
FRO-Jul13 Zn10	2.8-10.9	1-3.9	Zn-O	6.0	2.03±0.01	0.009±0.001	1.4 ± 0.1	0.70	0.0005
			Zn-Zn	1.2±0.3	3.122±0.01	0.0075±0.001			
			Zn-O	2±0.5	3.76±0.02	0.0075±0.005			

Table 5. FRO-DEC12 - EXAFS fitting parameters, shell by shell fitting using theoretical backscattering curves for the SPM sample FRO-Dec12 before and after Zn sorption. Summary of the local structural parameters derived from EXAFS data analysis (shell by shell fitting). The Zn EXAFS data were Fourier transformed over the k range Δk and fitted over the ΔR range with single scattering paths involving O, Zn or Al atoms. The amplitude reduction factor S_0^2 was fixed to 0.7 but the energy shift was released for fitting. The number of atoms of the first coordination shell was fixed to 6. The number of atoms, the distance R and disorder σ^2 were released for all the coordination shells. Parameters with strong correlation factors were not released simultaneously.

	Fitting range Δk(Å^{-1})	Fitting range ΔR (Å)	shell	Number of atoms	R(Å)	σ^2 (Å^2)	ΔE (eV)	S_0^2	R factor
FRO-Dec12	2.8-10.6	1.25-4.3	Zn-O	6.0	2.09±0.01	0.009±0.0005	6.9 ± 0.2	0.70	0.0007
			Zn-Zn	1.4±0.7	3.14±0.02	0.006±0.0005			
			Zn-Al	2±0.8	3.13±0.04	0.01±0.001			
			Zn-Zn	1±0.3	3.89±0.01	0.008±0.001			
			Zn-O	6±2	4.00±0.01	0.009±0.001			
FRO-Dec12 Zn2	2.8-11	1-3.5	Zn-O	6.0	2.05±0.005	0.0815±0.005	3.7 ± 0.2	0.7	0.0003
			Zn-Zn	2±0.5	3.13±0.01	0.008±0.001			
			Zn-Zn	0.7±0.5	3.34±0.01	0.010±0.001			
			Zn-O	2	3.93±0.01	0.01±0.001			
FRO-Dec12 Zn7	2.9-11	1-3.9	Zn-O	6.0	2.03±0.005	0.009±0.001	1.6 ± 0.1	0.7	0.0005
			Zn-Zn	1.5±0.5	3.10±0.01	0.006±0.001			
			Zn-Zn	0.7±0.5	3.27±0.01	0.01±0.001			
FRO-Dec12 Zn10	2.9-11	1.2-3.8	Zn-O	6.0	2.04±0.01	0.009±0.001	1.6 ± 0.1	0.7	0.0003
			Zn-Zn	1.5±0.5	3.12±0.01	0.007±0.001			

figure 8

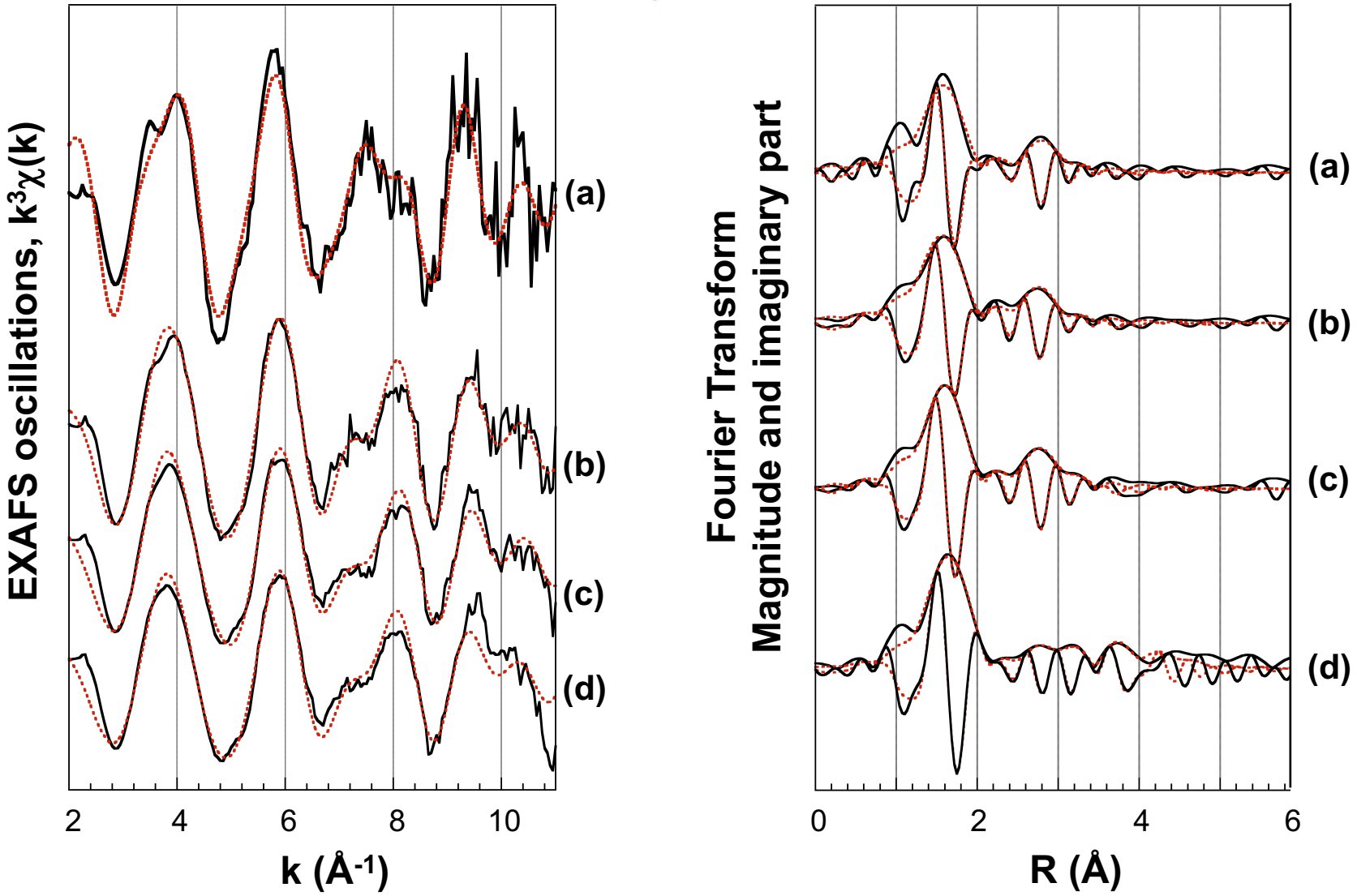
EXAFS oscillations, k³χ(k)
(a)
(b)
(c)
(d)
2
4
6
8
10
k (Å-1)
Fourier Transform
Magnitude and imaginary part
(a)
(b)
(c)
(d)
0
2
4
6
R (Å)